Post-Print

This is the accepted version of:

The final publication is available at https://doi.org/10.1016/j.actaastro.2020.07.003

Access to the published version may require subscription.

When citing this work, cite the original published paper.

Permanent link to this version
http://hdl.handle.net/11311/1146212

A New Strategy for the Reinforcement of Paraffin-based Fuels Based on Cellular Structures: the Armored Grain - Mechanical Characterization

Riccardo Bisin[a,∗], Christian Paravan[a], Sebastiano Alberti[a], Luciano Galfetti[a]

[a]Department of Aerospace Science and Technology, Politecnico di Milano, 34 via LaMasa, I-20156, Milan, Italy

Abstract

Paraffin waxes have been identified as promising hybrid rocket fuels. Though attractive from the ballistic point of view, these materials feature poor mechanical properties and, in particular, a brittle behavior making them unsuitable for application in operating systems. This study introduces a new strategy to enhance the mechanical properties of paraffin-based fuel grains manufactured at lab-scale. The implemented technique is based on the use of a 3D printed reinforcing structure embedded in the paraffin wax matrix and providing mechanical properties to the grain. This is named *armored grain*. The gyroid, a triply periodic cellular structure, is selected as a suitable reinforcing structure and its mechanical behavior is assessed by experimental and numerical investigations. Different 3D printable materials are considered, focusing the analysis on the differences due to their structural properties, compatibility and wettability with the paraffin fuel.

[∗]Corresponding author

Email addresses: `riccardo.bisin@polimi.it` (Riccardo Bisin), `christian.paravan@polimi.it` (Christian Paravan), `sebastiano.alberti@mail.polimi.it` (Sebastiano Alberti), `luciano.galfetti@polimi.it` (Luciano Galfetti)

In this paper, the mechanical properties of the gyroid-reinforced grains are evaluated by compression tests. The armored grains performance is compared to the mechanical behavior of fuel formulations in which reinforcement is pursued by blending the paraffin with thermoplastic polymers. The strength of the paraffin wax can be slightly enhanced by the addition of thermoplastic polymers. Under the investigated conditions (polymer mass fraction $\leq$ 10%), this reinforcing strategy yields blends with brittle behavior, while the armored grain provides a ductile behavior. The structural response of the armored grain can be tuned by exploiting different 3D printer polymers and relative densities (7%, 10%, 15%) for the gyroid reinforcement. Under the investigated conditions, the higher the relative density the stronger the mechanical properties. Albeit all the investigated polymers for gyroid reinforcement enhance the structural behavior of the paraffin wax, the nylon-based armored grain seems the most promising solution, featuring a 35% yield stress and a 296% yield strain increase over the paraffin baseline.

Nomenclature

Acronyms and Abbreviations

ABS	Acrylonitrile-Butadiene-Styrene
CB	Carbon Black
DSC	Differential Scanning Calorimetry
FDM	Fused Deposition Modeling
FEA	Finite Element Analysis

2

HRE	Hybrid Rocket Engine
HTPB	Hydroxyl-Terminated PolyButadiene
NY	Nylon 6
PLA	Polylactic Acid
S05W1	Blend of 94% SasolWax 0907, 5% SEBS and 1% CB
S10W1	Blend of 89% SasolWax 0907, 10% SEBS and 1% CB
SEBS-MA	Styrene-Ethylene-Butylene-Styrene copolymer grafted with Maleic Anhydride
SPLab	Space Propulsion Laboratory
TG	Thermogravimetry
W1	Blend of 99% SasolWax 0907 and 1% CB

Latin Symbols

a_E, n_E	Pre-exponential and exponential factors in Young modulus scaling law in Eq. (8)
a_σ, n_σ	Pre-exponential and exponential factor in yield stress scaling law in Eq. (9)
E	Young modulus, MPa
L	Gyroid cubic unit cell size, mm
m	Mass, g
r_f	Solid fuel regression rate, mm/s
T	Temperature, °C
$T_{end,m}, T_{end,deg}$	Melting and degradation end temperatures, °C
T_g	Glass transition temperature, °C
$T_{on,m}, T_{on,deg}$	Melting and degradation onset temperatures, °C
W_a	Ideal work of adhesion, mJ/m^2

Greek Symbols

σ	Stress, MPa
σ_y	Stress at yield, MPa
ϵ	Strain, %
ϵ_y	Strain at yield, %
η	Dynamic viscosity, Pa·s
γ	Surface free energy, mJ/m^2
γ^p, γ^d	Polar and dispersion components of the surface free energy, mJ/m^2
γ_L	Surface tension (liquid state), mN/m
γ_{CR}	Critical surface tension, mN/m
ρ	Density, g/cm^3
$\tilde{\rho}$	Relative density of a cellular structure
$\tilde{\rho}_\%$	Percent relative density of a cellular structure, %

1. Introduction

Hybrid rocket engines (HREs) are thermochemical propulsion systems featuring an intermediate configuration with respect to solid propellant motors and liquid rocket engines. Typically, in a HRE the fuel is solid and the oxidizer is liquid. Hybrid rocket engines offer a relatively easy hardware implementation enabling operating flexibility while granting high gravimetric specific impulse and intrinsic safety [1]. In addition to this, HREs enable reduced environmental impact operations with respect to solid rocket motors based on Cl-containing oxidizers [1, 2]. On the other hand, conventional (polymeric) HRE fuels feature slow regression rate (r_f) as a consequence of the complex combustion mechanism with convection heat transfer from the diffusion flame to the gasifying fuel [3–5]. Due

4

to this, simple grain geometries (i.e., cylindrical grains with circular central port perforation) yield low thrust levels, hence hampering the hybrid rocket technology implementation in boost applications and launch systems. Different strategies have been proposed to cope with this drawback [6]: burning surface area increase, turbulence enhancement in the combustion chamber, energetic additives addition, and the use of liquefying fuels, such as paraffin waxes [7]. Paraffin-based fuels represent a low-cost and effective solution for the r_f enhancement thanks to the entrainment phenomenon [8, 9]. However, paraffin wax alone is a brittle, low strength material, unsuitable to withstand most of the operating profile loads associated to launch system operations [10], or long time storage [11]. Thus, the research activity on paraffin-based fuels aims at designing formulations featuring suitable mechanical properties and high ballistic performance thanks to entrainment, which is promoted by low viscosity and low surface tension of the melted fuel [12]. The strengthening of paraffin mechanical properties is typically pursued by blending the wax with reinforcing binders (i.e., thermosetting or thermoplastic polymers) [13–17]. This method yields increased mechanical performance at the cost of enhanced melt fuel viscosity, with consequent entrainment and r_f reduction during the combustion.

The current study discusses an innovative strategy for the strengthening of paraffin-based formulations: increased mechanical properties are pursued by the use of reinforcing structures that are embedded in the paraffin fuel grains. Wax is the main fuel component promising fast r_f thanks to its relatively low melt-phase viscosity, while the enhancement of the paraffin-based grain structural behavior is provided by a cellular structure [18, 19] that is expected to turn the paraffin mechanical response from brittle to a ductile. The reinforcing structure considered

5

in this work is the gyroid, a triply periodic cellular structure with open-cells [20–23]. The gyroid is produced by additive production (AM) exploiting fuse deposition modeling (FDM). The AM has already been presented as a method for fuel grain manufacturing [24–26], and for the creation of scaffold structures embedding paraffin [27–29]. In previous open literature works, the 3D printed grain from AM was considered as the main fuel grain component. In the current study, the FDM printed gyroid is intended as a reinforcing structure with a limited mass fraction with respect to the paraffin fuel. The strategy for the use of the FDM printed gyroid in the paraffin grain is similar to the civil engineering use of reinforced concrete. The combination of gyroid structure and paraffin fuel is hereby called the *armored grain*.

In the paper the mechanical properties of 3D printed gyroids, paraffin and armored grains are investigated experimentally by compression tests. Finite element analysis (FEA) is applied for the evaluation of the mechanical behavior of gyroids. Reinforcing structures are printed by different thermoplastic polymers whose characteristics are evaluated in terms of slow heating rate thermal behavior [differential scanning calorimetry (DSC) - thermogravimetry (TG)] and compatibility with the paraffin fuel.

2. Background

2.1. Paraffin-based Fuel Reinforcement

Paraffin-waxes are liquefying fuel formulations [8, 9] featuring a thermoplastic behavior. Thermoplastic materials offer some advantages when considering grain manufacturing cost reduction. Differently from thermosetting materials, thermo-

plastics do not require long curing times. Moreover, in the case of production of a fuel grain not meeting the requirements, thermoplastic formulations may be re-melted, thus reducing production costs as well as industrial wastes. Different open literature works focus on the strengthening of paraffin-waxes mechanical proper-ties. In these analyses, the reinforcing materials are used to create a binding ma-trix hosting wax pockets, or blending the paraffin with strengthening agents. The key point of these reinforcing methods is the remediation of the brittle and frail behavior of wax with limited alterations of its original low viscosity [16, 30, 31].

Conventional (i.e., non-liquefying) fuels as hydroxyl-terminated polybutadi-ene (HTPB) feature high mechanical properties, though the r_f is limited. Their use as reinforcing binders for fast-burning paraffin wax was one of the first meth-ods proposed for the creation of a fuel formulation with suitable mechanical and ballistic properties [13–17, 31–38]. Boronowsky [32] tested the combustion be-havior of paraffin, HTPB and two different heterogeneous HTPB-based fuels con-sisting of 15 wt% and 30 wt% granulated paraffin chunks (with size in the range 0.3-0.7 mm). The rationale was the HTPB r_f enhancement by embedding pockets of paraffin that could be entrained during the combustion. The addition of 15% and 30% paraffin led to 25% and 40% average r_f enhancement when compared to standard HTPB. Even though quantifiable experiments inspecting the structural capabilities were not performed, the fuel with 15% of wax was reported to be as re-silient as plain HTPB. On the other hand, grain structural integrity appeared jeop-ardized by the addition of 30% paraffin to the polyurethane. Sisi and Gany [13] carried out firing tests on paraffin, polymethyl methacrylate (PMMA) and a mixed fuel consisting of a HTPB binder filled with synthetic paraffin particles (0.5 mm diameter). Cylinders of 30 mm diameter and 50 mm length were tested at com-

7

pression with a displacement rate of 5 mm/min. The HTPB-reinforced paraffin fuels featured improved elasticity compared to plain paraffin. The HTPB-based blends exhibited slower r_f than the plain paraffin formulation, though the r_f still showed a two- to three-fold increase with respect to PMMA. Paraffin-wax-based fuels reinforced by HTPB were tested by Thomas et al. [14]. In this latter study, the authors focused on HTPB, paraffin, and HTPB loaded with 10, 25, 50, and 75 wt% of paraffin. The combustion tests were carried out in gaseous oxygen by a lab-scale hybrid rocket. Considering HTPB as the baseline for the relative grading, the plain paraffin fuel exhibited a r_f increase of 300%, while the HTPB-paraffin mixed fuels showed no ballistic performance enhancement. Possible explanations for the dissimilar ballistic responses observed in Refs. [13, 14, 32] include differences (i) in the ingredients and the manufacturing procedures (e.g., use of molten paraffin wax or granules, curing ratio of the HTPB binder), and (ii) in the investigated operating conditions. Improvement of paraffin fuel mechanical properties and, in particular, of its elongation at break was achieved by Wang et al. [33] adding organically modified montmorillonite (OMMT), a phyllosilicate that is the main component of clay. Young modulus and tensile strength were enhanced and 450% increase of elongation at break was achieved thanks to a 2 wt% of OMMT. Kobald et al. [34] investigated the mechanical properties and the burning behavior of different paraffin-waxes blended with stearic acid (SA), nanoclay and a not specified polymer. The addition of additives increased the melted fuel viscosity under reference conditions (liquid phase rheology being tested at 120°C), with effects on both the mechanical and r_f performance of the formulations. With pristine paraffin wax as baseline, the tensile strength and maximum elongation at break of the blend with 10 wt% polymer showed two- and three-fold

8

increases, respectively, while r_f was halved. Paraffin-polyethylene (PE) blends were evaluated as a suitable reinforcing solution thanks to the thermoplastic polymer compatibility with alkanes [35]. A blend with 5 wt% PE featured a 25% tensile strength enhancement and a 34% compression strength increase with respect to paraffin. The same properties gained 42.4% and 42.2%, respectively, with 10 wt% PE. Different mass fractions of ethylene-vinyl acetate (EVA) were added as strengthening agent to pure paraffin by Maruyama et al. [15]. The 20 wt% blend showed an increase of 1.6 times in the tensile stress and of 2.3 times in the tensile strain. As a drawback, the viscosity increased of six times and the measured r_f decreased by ≈35% with respect to the pure paraffin taken as a baseline. Kumar and Ramakrishna [36] also improved the mechanical properties of wax by adding 10 wt% and 20 wt% of EVA. The tensile strain increased by 17% for the 20% EVA loaded wax formulations. The tensile strength was also enhanced. The r_f decrease due to the augmented melt fuel viscosity was compensated by exploiting a bluff body at the motor head end, leading to a r_f 3.5 times higher than the one obtained with polymeric fuels. The effects of mechanical properties reinforcement by styrene-ethylene-butylene-styrene copolymer grafted with maleic anhydride (SEBS-MA) were extensively studied at SPLab [16, 31, 37]. The tensile tests were carried out on macro- and micro-crystalline waxes and paraffin-polymer blends featuring different mass fraction of SEBS-MA, ranging from 5% to 40%, at crossbar speeds of 0.5 and 50 mm/min, with temperatures of 8°C and -19°C [16, 37]. Increasing the SEBS-MA content yielded a decrease of the Young modulus. The test temperature decrease had a positive influence on the mechanical behavior, increasing both the maximum load and the elongation at break [16]. For SEBS-MA mass fractions higher than 20%, the samples featured

9

a ductile behavior, resulting in elongation at break enhancement. The addition of SEBS-MA implied also a significant melt fuel viscosity enhancement (40% SEBS-MA addition yielded a viscosity value 400-500 times the one of the pure paraffin). The viscosity increase strongly hindered the entrainment capability and lowered the ballistic performance of the fuels. A power law correlation between the regression rate r_f, normalized to the HTPB baseline, and the fuel viscosity was retrieved [16, 31]. This evidence highlighted the strong sensitivity of r_f on the viscosity and the importance of a detailed rheological analysis of the solid fuels. Tang et al. [17] tested paraffin blends with 5 wt% of different strengthening agents including stearic acid, polyethylene wax, ethylene-vinyl acetate, low density polyethylene (LDPE), polypropylene (PP) and high density polyethylene (HDPE). Compression and tensile tests were conducted. The best results in terms of compression and tensile strength were achieved by polyethylene wax (64.0% increment) and by LDPE (105.3% increase), respectively. Combustion tests were performed inspecting the negative influences of reinforcing additives on the r_f. The proposed power law correlation between the r_f and the melted liquid viscosities was in agreement with Refs. [16, 31]. The use of polyurethane foam (PUF) as a reinforcing matrix hosting liquid paraffin is discussed in Ref. [38]. The investigated PUF featured cells with characteristic size in the range 300-400 μm, with a density of 0.02 g/cm^3. Energetic additives, such as lithium aluminum hydride, magnesium hydride and aluminum, were also added to the fuel formulations. The PUF-reinforcing strategy led to a fuel featuring attractive r_f, though the stochastic foam structure implied anisotropic mechanical properties.

Studies on the effects of energetic fillers on the mechanical properties of wax-based formulations are reported in Refs. [39–41]. All these works deal with the

10

same (microcrystalline) paraffin wax, SasolWax 0907. Paraffin-waxes loaded with micron- and nano-sized *Al* powders (nominal particle size of 8 μm and 100 nm, respectively) exhibited increased tensile and compression performance [39]. Veale et al. [40, 41] investigated SasolWax 0907 with 40 wt% of μ*Al* at different temperatures (23°C, 30°C and 40°C) and strain rates (1, 10 and 100 mm/min). The ultimate tensile strength (UTS) of the tested materials was found to raise for increasing strain rate, while the corresponding elongation decreased. The trend was reverted when increasing the tested specimen temperature. Such a change turned the paraffin-behavior from brittle to ductile.

Nowadays, AM has been applied to hybrid rocket fuels. It enables a fast and relatively cheap production of polymeric fuel grains with standard/complex grain geometries [24]. Conventional HTPB fuel grains manufactured by casting procedure were compared with FDM-produced acrylonitrile-butadiene-styrene (ABS) 3D printed fuels in [25]. Firing tests were performed with nitrous oxide as oxidizer. The printed fuel featured a slightly reduced r_f performance with respect to the HTPB baseline. McFarland and Antunes performed small-scale burning tests of 3D printed cylindrical central-perforated fuel grains [26]. Different printing materials were considered, with acrylonitrile styrene acrylate (ASA) and nylon fuels featuring the highest regression rates. Another application of additive manufacturing consists in using printed structure as support for paraffin fuels. McCulley et al. manufactured hollow ABS grains which were later filled with paraffin [27]. The ABS support structure hosted the paraffin (25% of the grain mass) that served as an additive to improve the r_f of the fuel grain. The firing test results did not match the theoretical predictions suggesting the presence of unburned paraffin fuel expelled from the ABS structure. Armold et al. [28, 29] investigated paraffin in a

11

twisted honeycomb structure printed in acrylic. The study focused on the enhancement of the r_f and combustion efficiency thanks to the increase of the initial fuel grain temperature. Neither McCulley et al. [27], nor Armold et al. [28, 29], conducted mechanical tests on their grains and, to the best knowledge of the authors, no quantitative information on the mechanical properties of structure-reinforced paraffin-based fuel grains is available in the open literature.

2.2. Cellular Structures and the Gyroid

This work studies the fuel grain reinforcement effects of paraffin-based formulations embedding 3D printed cellular structures in the alkane wax matrix. Cellular structures are connected networks of struts with periodic or stochastic arrangements of cells. This class of structures (also known as cellular solids, or lattice materials) include foams, honeycomb and regularly repeating lattice structures [18, 19]. The characteristics of a cellular solid depend on (i) the properties of the material the lattice is created from, (ii) the structure topology and the shape of the cell edges, and (iii) the relative density $\tilde{\rho}$, defined as the ratio between the density of the lattice ρ (i.e., the lattice structure mass divided by the enveloped volume) and the density of the solid material ρ_{bulk}.

The mechanical behavior of lattice materials classifies them into bending- and stretch-dominated structures [19]. Bending-dominated structures respond to applied loads by the bending deformation of the struts composing the cell. In these structures the compressive stress (σ)-strain (ϵ) curve features an elastic behavior until a yield limit. This is then followed by an almost constant $\sigma(\epsilon)$ (plateau stress) with densification. In the stretch-dominated structures the cell edges stretch instead of bending. For these structures the typical $\sigma(\epsilon)$ shows a post-yield softening before the densification. Examples of bending- and stretch-dominated struc-

12

tures are foams and honeycombs, respectively.

Scaling laws are proposed for the definition of the mechanical behavior of cellular structures [19]. The Young modulus (E) and the yield stress (σ_y) of the lattice structure are related to the properties of the bulk material (E_{bulk}) through the relative density $\tilde{\rho}$. The Young modulus scales as:

$$\frac{E}{E_{\text{bulk}}} \propto \left(\frac{\rho}{\rho_{\text{bulk}}}\right)^2 = \tilde{\rho}^{\,2} \quad \text{(bending-dominated behavior)} \tag{1}$$

$$\frac{E}{E_{\text{bulk}}} \propto \left(\frac{\rho}{\rho_{\text{bulk}}}\right) = \tilde{\rho} \quad \text{(stretch-dominated behavior)} \tag{2}$$

Concerning the yield stress, the scaling law is typically presented in the form:

$$\frac{\sigma_y}{E_{\text{bulk}}} \propto \left(\frac{\rho}{\rho_{\text{bulk}}}\right)^2 = \tilde{\rho}^{\,2} \tag{3}$$

Equation (3) is independent from the structure topology (i.e., bending- or stretch-dominated) and it is valid under the assumption of slender struts undergoing buckling before yield.

The identification of a suitable reinforcing structure for the paraffin fuels is based on (i) the presence of open cells, (ii) uniformity, (iii) efficiency of volume usage, and (iv) prototyping promptness. Open cells are preferred to provide an easy casting of the melt paraffin fuel in the reinforcing structure and to grant paraffin availability during the combustion. Uniformity of the lattice is required to provide an isotropic mechanical behavior and to prevent anisotropic combustion with random disposition of the cells (even though the structure is supposed to burn, the actual fuel shall be paraffin). For this reason, a moderate volume fraction of reinforcing material (also called infill) should be selected to provide good mechanical properties. The structure is also required to be easy and fast to obtain

13

with a 3D printer.

The *gyroid* has been identified as a suitable scaffold structure for the reinforcement of the paraffin-based fuel grains. The gyroid is an open-cell structure featuring a minimal surface for a given volume. This enables a high filling efficiency of the cells volume in the lattice (i.e., a wide paraffin availability during burning). Moreover, the gyroid is an easy printable shape featuring a triply periodic structure. This feature grants high uniformity, minimizing the anisotropy in the mechanical properties and avoiding stress concentrations. The gyroid was firstly studied by Schoen in 1970 [20] and, nowadays, it finds application in different fields spanning from curtain wall design [42] to tissue engineering [43]. The parametrization of the gyroid involves elliptic integrals [20], however, a close approximation to the gyroid surface (see Ref. [44]) is given by:

$$\sin\left(\frac{2\pi x}{L}\right)\cos\left(\frac{2\pi y}{L}\right) + \sin\left(\frac{2\pi y}{L}\right)\cos\left(\frac{2\pi z}{L}\right) + \sin\left(\frac{2\pi z}{L}\right)\cos\left(\frac{2\pi x}{L}\right) = 0 \qquad (4)$$

In the Eq. (4), L is the unit cell size of the cube the single gyroid cell can be inscribed in (see Fig. 1). In an actual gyroid, a layer thickness (d) is associated to the surface to create the cellular solid. The gyroid lattice is generally produced by additive manufacturing because of its complex geometry. Yan et al. [21] fabricated gyroid lattices of 15% volume fraction using the selective laser melting process. Finite element analyses of the gyroid are discussed in Ref. [45]: results show the reduced anisotropy of the gyroid lattice with respect to other cellular structures, and the possibility of implementing a density-based topology optimization for designing functionally graded cellular structures with desired mechanical properties. Qin et al. [22] tested gyroid-shaped graphene assemblies, as well as 3D printed gyroid structures realized in VeroMagenta. The two series of gyroids showed the

14

same scaling laws, thus suggesting an independence of the latter from the considered materials. Maskery et al. [23] examined three types of lattices: gyroid, diamond and primitive. Mechanical tests and finite element calculations were performed. Primitive lattice exhibited a stretch-dominated behavior, while the gyroid and diamond lattice deformed in a bending-dominated manner.
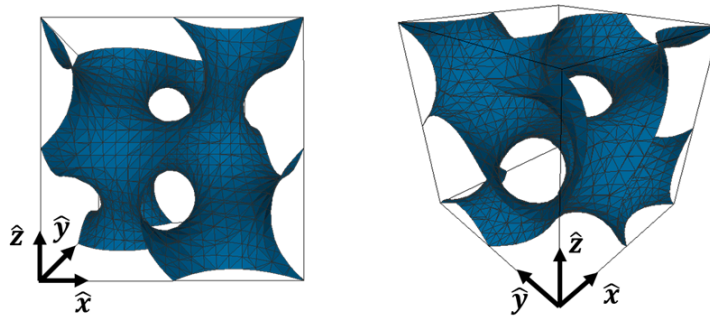

Figure 1: Different views of a gyroid cell.

3. Investigated Materials

The fuel formulations considered in this study are based on a commercial microcrystalline paraffin wax, SasolWax 0907. This material is produced by Sasol GmbH (Germany) [46]. SasolWax 0907 has already been considered as a candidate for hybrid rocket propulsion applications [31, 34, 47, 48] in light of its relatively high thermal stability. The average chemical composition of this ingredient is $C_{50}H_{102}$ and it consists of 36% linear (n-) alkanes and 64% branched alkanes (isoalkanes). The oil content is lower than 1-2%, the congealing point is 83-94°C, while the density is 0.924 g/cm^3 [46, 48]. The baseline for the relative grading of the mechanical properties of the investigated fuel grains is the fuel for-

mulation W1 (see Table 1). The reinforcement of the pure paraffin formulation is pursued by two different strategies: (i) paraffin-blending with SEBS-MA, and (ii) embedding gyroid structures in pure paraffin matrices to create armored grains. All the tested fuel formulations include 1 wt% carbon black (CB) as an opacifier of the solid fuel grains, in the perspective of their use in ballistic tests. The tested CB features a particle size <20 μm [49].

3.1. Paraffin-based Blends

The reinforcing material for blending is a thermoplastic copolymer, SEBS-MA. A wide characterization of SEBS-MA-containing fuels prepared starting from different paraffin waxes is reported in Ref. [16]. The SEBS-MA is characterized by high mechanical and thermal properties [50]. In the copolymer, the central ethylene-butylene block is responsible for the rubber-like consistency of the material, styrene monomers confer to SEBS its thermoplastic behavior [16]. The copolymer features a density of 0.910 g/cm^3. The investigated paraffin-based fuel blends are listed in Table 1 together with their detailed compositions and viscosities [30].

3.2. Armored Grains

Armored grains are produced embedding the gyroid structure in the W1 paraffin fuel grains. Three different thermoplastic polymers have been used to build the gyroid cellular structure by FDM: polylactic acid (PLA), ABS, and nylon 6 (NY). The filaments for the FDM printing were supplied by Prusa (PLA and ABS) [51], and Filoalfa (NY) [52].

The PLA is a biodegradable and sustainable thermoplastic aliphatic polyester, derived from renewable resources [53]. The PLA is widely used in FDM because

16

Table 1: Investigated paraffin-based blends.

Fuel	Ingredients, [wt%]			Dynamic viscosity[a], η [Pa·s]
	SasolWax 0907	SEBS-MA	CB	
W1	99	0	1	0.005 ± 0.000[b]
S05W1	94	5	1	0.014 ± 0.001
S10W1	89	10	1	$0.040 \pm$ NAv.

[a] Plate-plate geometry, shear rate 1000 s^{-1}, T=150°C.

[b] For W1, over three measurements, the confidence interval is < 0.001.

it is easy to print and relatively cheap. In spite of some complications related to the printing (warping, bed adhesion issues), ABS is commonly employed in FDM thanks to its good mechanical and thermal properties. In particular, ABS was characterized as fuel for hybrid rocket applications [25], and 3D printing was exploited for the manufacturing of solid fuel grains with non-conventional port geometries [54] or grain configurations [24]. Nylon 6 is a thermoplastic polymer featuring high toughness and flexibility together with good thermal characteristics. The main issue related to the use of NY is its tendency to absorb moisture in wet environments (water absorption is 3.20% at 23°C and relative humidity of 50% [52]). Moreover, NY-printing suffers from warping due shrinkage stresses generated from the NY crystallization during the print cooling phase. As a consequence, NY-printed components typically show reduced mechanical properties with respect to the bulk material. To solve this problem, NY-filaments could be doped with additives to modify the crystallization process and reduce the shrinkage stresses [55]. In the current study all filaments were stored under controlled conditions (dry environment-RH <10%, 25°C).

Table 2 provides an overview of the gyroids and armored grains configurations considered in the analysis. The effects of the printed structure infill on the reinforcing structure mechanical properties were assessed testing PLA-printed gyroids with relative densities in the range 7% to 15%. Armored grains prepared with PLA gyroids enable to evaluate the effects of the reinforcing structure infill on the paraffin grain reinforcement. The influence of the printed polymer on the armored grain behavior was investigated contrasting the performance offered by PLA, ABS, and NY gyroids with 15% nominal infill (see Table 2).

Table 2: Investigated gyroid structures and armored grains.

Specimen ID	Gyroid material	Nominal infill	W1	Notes	
PLA_i07	PLA	7%	NO	Infill effects on the gyroid structures,	
PLA_i10	PLA	10%	NO	specimens ID will be adapted according to	
PLA_i15	PLA	15%	NO	the manufacturing procedure (Section 4.1)	
W1_PLA_i07	PLA	7%	YES	Infill effects on	The same manufac-
W1_PLA_i10	PLA	10%	YES	the armored grains	turing procedure is
W1_PLA_i15	PLA	15%	YES		adopted for all
W1_ABS_i15	ABS	15%	YES	Gyroid material effects	the specimens
W1_NY_i15	NY	15%	YES	on the armored grains	(Section 4.1)

4. Methodology

The characterization and comparison between the two paraffin grains reinforcing strategies (blend and armored grain) were pursued through different steps. The production of gyroid lattice is presented along with the manufacturing process

of both paraffin blends and armored grains. The experimental test campaign involved thermogravimetric analyses and materials compatibility studies to characterize the raw components of the fuels. The structural behavior of paraffin blends and armored grains were investigated by compression tests. Finite element analysis (FEA) revealed to be an useful tool to predict the lattice structure behavior.

4.1. Gyroid Production

The gyroids were printed by means of a commercial FDM 3D printer (Prusa i3 MK3 [51]) using two different methods: (i) setting the gyroid infill pattern provided by the native (open-source) slicer of the printer, and (ii) exploiting the equation describing the gyroid surface [Eq. (4)]. For the sake of clarity, the gyroid generated with the first procedure is called the *infill gyroid*, while the one obtained by the second method is the *SPLab gyroid*.

The design parameter of the *infill gyroid* is the infill, that is the percentage showing how much a solid model is filled in with material when printed. In this work, the infill coincides with the percent relative density ($\tilde{\rho}_\%$). The gyroids printed exploiting this method feature a strut thickness (d) of 0.45 mm, that is equal to the extrusion width of the 3D printer. Considering the *SPLab gyroid*, different surfaces are generated in MATLAB by tuning the *L* parameter [see Eq. (4)]. The surfaces are then thickened to $d = 0.45$ mm, and printed. A correlation between *L* and $\tilde{\rho}_\%$ was retrieved (Table 3), hence a perfect match between *infill gyroid* and *SPLab gyroid* was achieved from the geometrical point of view, as shown in Fig. 2 (slicer view) and in Fig. 3 (printed structures). One the other hand, some differences can be appreciated between the two production methodologies. *Infill gyroids* are characterized by the presence of extra material attached to the external perimeter of the printed gyroid and by open saddle points, as shown in Fig. 4a.

Conversely, the *SPLab gyroid* method is characterized by a fragmented print and by a non-continuous path for the 3D printer extruder, in turn, leading to some imperfections around the aforementioned saddles points (see Fig. 4b). Despite the geometrical consistency of the two approaches, Table 3 highlights a gap between the actual relative densities of the *infill* and *SPLab gyroids*, due to the presence of saddle points. It should be also noted that the infill values are equivalent to the relative densities of the *infill gyroids*. Concerning the *SPLab gyroids*, the infill values slightly differ from the $\tilde{\rho}_\%$. The reason for this inconsistency is that the input parameter for the *SPLab gyroid* production is L instead of the infill.

Infill gyroid approach has been selected as the gyroid manufacturing procedure for the armored grains. In fact, *infill gyroid* is optimized for the 3D printing (flaws and defects are minimized since the gyroid pattern is already implemented in the native slicer) and the printing time is shorter than the *SPLab gyroid*. The latter is used as the starting input for the FEA. This choice is due to the fact that the *SPLab gyroid* method provides a suitable and representative grid of points for the mesh generation. On the contrary, the *infill gyroid* is not appropriate for the FEA, since it does not provide the CAD model of the gyroid. In fact, this approach relies on the native slicer of the printer, whose rationale is filling an input volume with the desired pattern featuring the required infill percentage.

4.2. Fuel Grains Manufacturing

Mechanical tests were performed on cylindrical specimens with outer diameter of 30 mm, and height of 50 mm. The specimen shape and sizes comply with the ISO 604 standard [56]. Paraffin blends were prepared by melt casting in cylindrical molds. Details on the manufacturing of solid fuel blends are reported elsewhere [16]. A melt casting procedure was exploited for the armored grains

20

Table 3: Nominal infill percentage, gyroid unit cell size [Eq. (4)], and measured percent relative density for *infill* and *SPLab gyroid*.

| Nominal infill	Gyroid unit cell size, L [mm]	*Infill gyroid*, $\tilde{\rho}_\%$ [%]	*SPLab gyroid*, $\tilde{\rho}_\%$ [%]
7%	15.0	7.8 ± 0.1	8.4 ± 0.1
10%	10.5	10.2 ± 0.1	11.8 ± 0.1
15%	7.0	14.6 ± 0.1	17.5 ± 0.1
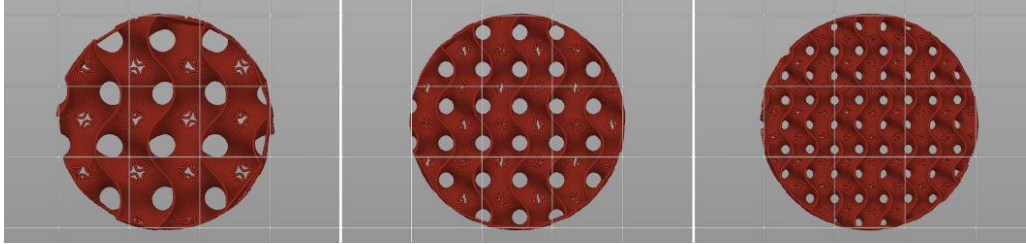
(a) *Infill gyroids*: I-PLA_i07, I-PLA_i10, I-PLA_i15 (from left to right).
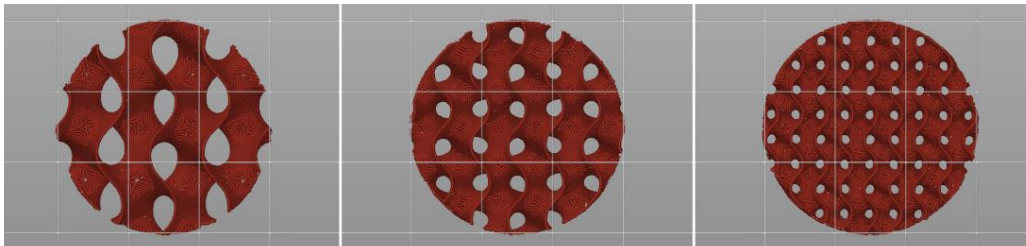
(b) *SPLab gyroids*: S-PLA_i07, S-PLA_i10, S-PLA_i15 (from left to right).

Figure 2: Slicer top previews of gyroids with 7%, 10%, 15% nominal infill (from left to right). Specimen sizes: 30 mm in diameter and 50 mm in height.
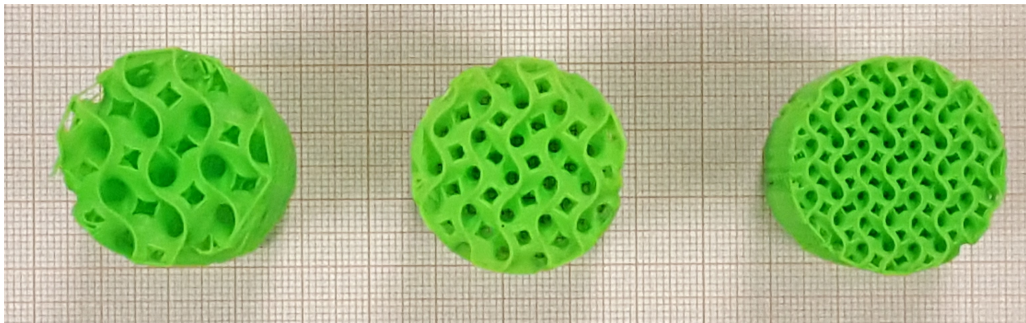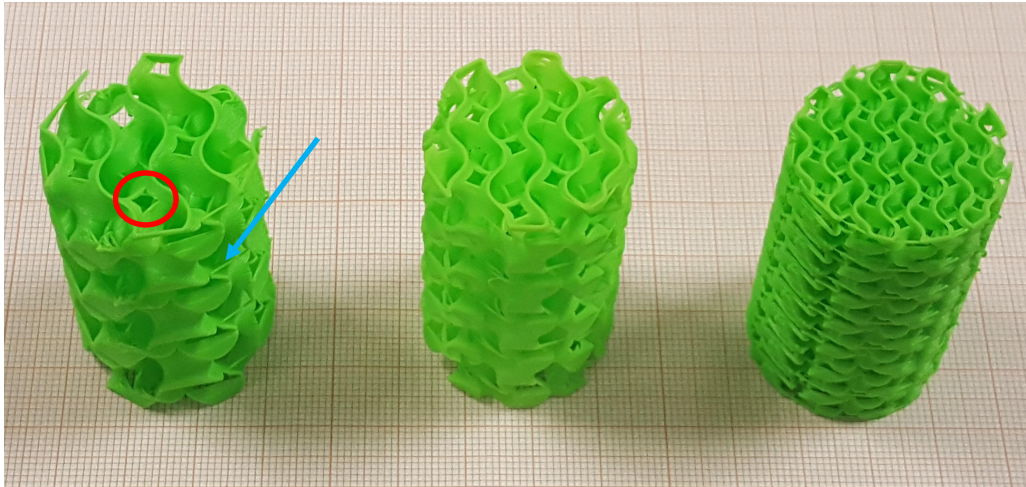
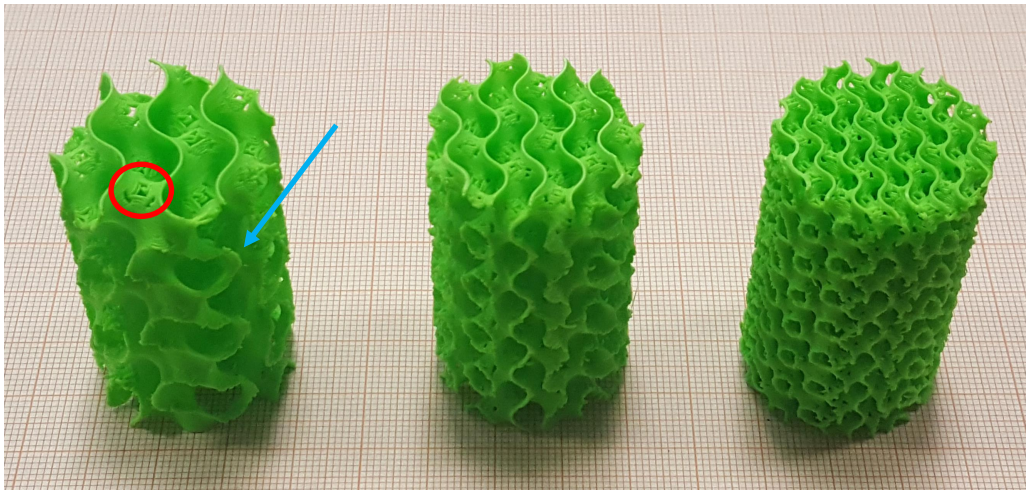(a) *Infill gyroids*: I-PLA_i07, I-PLA_i10, I-PLA_i15 (from left to right).

(b) *SPLab gyroids*: : S-PLA_i07, S-PLA_i10, S-PLA_i15 (from left to right).

Figure 3: Top views of 3D printed PLA gyroids with 7%, 10%, 15% nominal infill (from left to right). Specimen sizes: 30 mm in diameter and 50 mm in height.

(a) *Infill gyroids*: I-PLA_i07, I-PLA_i10, I-PLA_i15 (from left to right).

(b) *SPLab gyroids*: S-PLA_i07, S-PLA_i10, S-PLA_i15 (from left to right).

Figure 4: 3D printed PLA gyroids with 7%, 10%, 15% nominal infill (from left to right). Specimen sizes: 30 mm in diameter and 50 mm in height. Red circles and blue arrows show saddle points and printing defects respectively on the 7% gyroids.

too. Paraffin and paraffin-based formulations undergo a marked shrinkage during solidification [57]. This effect was contrasted by applying a pressure (<1.0 MPa) to all the fuel samples during the cooling and solidification phase.

4.3. Simultaneous Thermal Analysis (TG/DSC)

Simultaneous TG/DSC analyses were performed to characterize the thermal behavior of the W1 formulation, of the paraffin-based blends (see Table 1) and of the polymers used for the FDM of the gyroids (PLA, ABS, NY). Thermal analyses were carried out with a Netzsch STA 449 F5 Jupiter [58]. Tested specimen mass was 10.0 ± 0.5 mg. Scans were performed in an *Ar* flow (75 ml/min) with an heating rate of 10°C/min in the temperature range 25-800°C. Degradation onset and end temperatures were evaluated by the tangent method [59]. An example of onset and end temperature determination is reported in Fig. 5, that shows the thermal behavior of the ABS considered in the current study. While the TG trace provides information on the polymer mass loss due to gasification, the DSC gives details on the glass transition temperature, the melt temperature onset and the fusion enthalpy (if any) of the tested material.

4.4. Materials Compatibility and Wettability

The armored grain is a heterogeneous structure in which the gyroid is surrounded by solid paraffin. Thus, intimate contact and good adhesion between the two main armored grain components are required to prevent significant defects (e.g., voids inside the grain) and to maximize the cellular lattice impact on the mechanical properties enhancement. Wettability investigation is crucial for the armored grain manufacturing since it is produced by melted paraffin casting. Polymers and paraffin compatibility and wettability were studied measuring the
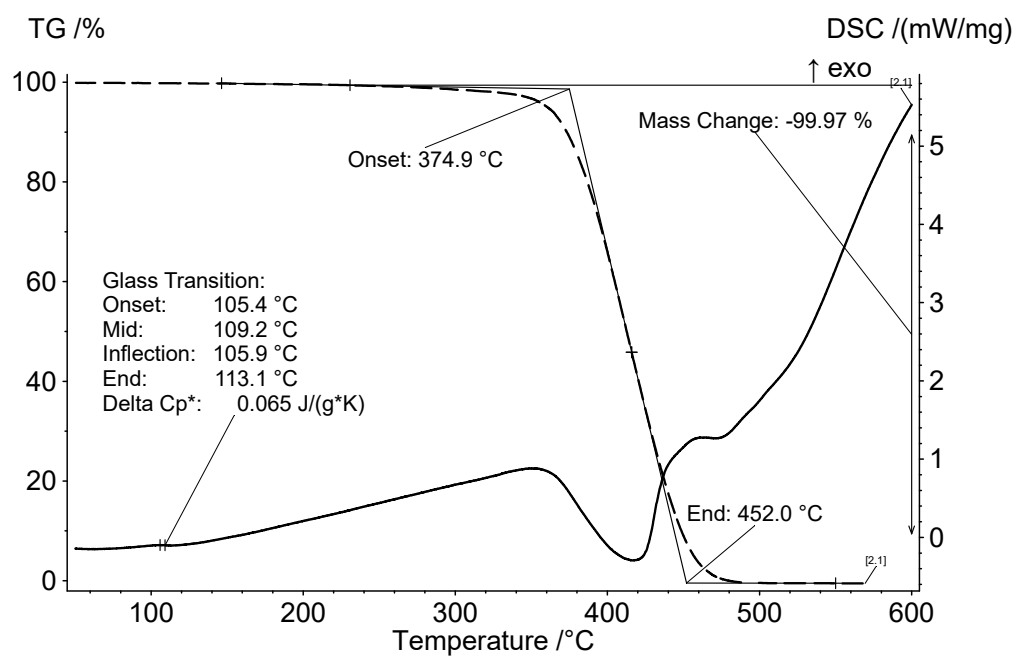
24

Figure 5: TG (dashed line) and DSC (solid line) traces for ABS (10°C/min, 75 ml/min *Ar*, 10.0 ± 0.5 mg). Note the absence of an endothermic melting peak due to the amorphous nature of the polymer.

critical surface tension (γ_{CR}) of the 3D printer polymers, their surface free energy (γ) and the polar (γ^p) and dispersion (γ^d) components. Even though the surface free energy and the surface tension are not numerically equivalent, the two terms are commonly used to describe the same property [60, 61]. In the present work, the term surface tension refers to the liquid state, while the term surface free energy is used when referring to the solid state.

Critical surface tension is defined as the surface tension at which a liquid completely wets the solid. According to Fox-Zisman method [62] an empirical linear relation was found between the cosine of the liquid-solid contact angle [$\cos(\theta)$] and the surface tension of a series of testing liquids. The intercept of the line at $\cos(\theta) = 1$ is the γ_{CR}. Contact angles were determined via sessile method [60]. The measurements were performed on 3D printed plates of the three different printer materials (PLA, ABS, NY). The plates were smoothed using a press at 5.0 ± 0.1 MPa to reduce surface roughness and hysteresis-capillarity penetration phenomena, affecting the results reliability.

The measurement of the surface free energy provides an overview of the adhesion between the W1 paraffin and the gyroids printed with the different polymers. The surface free energy and the polarity of the 3D printer polymers and the W1 were calculated according to the Owens-Wendt method [63]. This technique uses the contact angles of two testing liquids and the following equations:

$$[1 + cos(\theta_1)] \, \gamma_1 = 2 \left(\gamma_1^d \, \gamma_s^d\right)^{1/2} + 2 \left(\gamma_1^p \, \gamma_s^p\right)^{1/2} \tag{5}$$

$$[1 + cos(\theta_2)] \, \gamma_2 = 2 \left(\gamma_2^d \, \gamma_s^d\right)^{1/2} + 2 \left(\gamma_2^p \, \gamma_s^p\right)^{1/2} \tag{6}$$

In Eqs. (5) and (6), $\gamma = \gamma^p + \gamma^d$ and the subscripts 1, 2 and s refer to the testing liquids 1 and 2, and to the investigated solid state polymer. Water (H_2O)

26

and methylene iodine (CH_2I_2) were used as testing liquids since their γ^p and γ^d values are available in open literature ($\gamma^p_{H_2O}$= 51.00 mN/m, $\gamma^d_{H_2O}$= 21.80 mN/m; $\gamma^p_{CH_2I_2}$= 1.30 mN/m, $\gamma^d_{CH_2I_2}$= 49.50 mN/m) [60]. Equations (5) and (6) can be solved through algebraic manipulations [60] to evalute the γ^d and γ^p components and, therefore, the surface free energy $\gamma = \gamma^p + \gamma^d$. The ideal reversible work of adhesion (W_a) is defined as the free energy change required to separate the two phases. The work of adhesion W_a between two bulk phases α and β can be estimated as [63]:

$$W_a = W_a^d + W_a^p = 2\left(\gamma_\alpha^d \, \gamma_\beta^d\right)^{1/2} + 2\left(\gamma_\alpha^p \, \gamma_\beta^p\right)^{1/2} \tag{7}$$

where γ_α is the free surface energy of phase α, γ_β the surface free energy of phase β. In the present case, the two bulk phases are the two ingredients of the armored grain: W1 paraffin and the polymer the reinforcing structure is made of. As remarked by Wu [60], the ideal work of adhesion W_a could significantly differ from the real work of adhesion because of defects at the interface between the two phases. Nevertheless, the evaluation of the ideal work of adhesion can provide a relative grading between different paraffin-polymer couples.

4.5. Compression Testing

Uniaxial compression tests were conducted on paraffin grains, 3D printed bulk grains, gyroid lattices and armored grains. All the tests were carried out at ambient temperature ($T = 25 \pm 5$ °C) with compression rate of 1 mm/min. Four samples were tested per each type of specimen. Based on the sample sizes, results can be considered valid until a maximum strain of 14.4% is reached. Above this value, the specimen could undergo buckling [56]. The test campaign was conducted on a MTS 810 universal testing machine equipped with a 250 kN load cell.

4.6. Finite Element Analysis (FEA)

The mechanical behavior of the gyroid structures was investigated by FEA using Femap with NX Nastran [64]. Feasibility of FEA prediction of the gyroid mechanical properties and scaling laws was addressed. The simulations focused on compression tests and replicated the same operating conditions considered in the experimental part. Gyroids featuring 7%, 10%, 15% nominal infills and realized in PLA, ABS and NY were investigated. The analysis covered the elastic and plastic field, so a nonlinear analysis (SOL106) [65] was implemented. The CAD models of the gyroids were created following the *SPLab gyroid* approach. This choice was based on two considerations: (i) the geometrical similarity between *infill* and *SPLab gyroids*, and (ii) the impossibility of generating a CAD model or a mesh of the gyroid by means of the *infill gyroid* method. Finite element analysis consisted of the following steps.

1. **Gyroid mesh creation**. The FEA mesh was implemented exploiting the gyroid periodicity. In fact, the gyroid lattice is built by repetition of the lattice unit cell (see Fig. 1) and the final mesh was created assembling single fundamental repeating units.

2. **Elements and material definition**. For the FEA, 2D plate elements (Nastran CTRIA3 [65, 66]) were used and their thickness was set to 0.45 mm, as the default extrusion width of the 3D printed gyroids. Compression tests performed on the 3D printer bulk materials allowed the definition of the material properties for the FEA.

3. **Loads and constraints**. Simulations were based on the experimental compression test campaign. Thus, two rigid elements (RBE2 [66]) were created and connected to the top and bottom nodes of the specimen to model the

28

contact plates of the compression test. Rigid elements were also constrained in translation and rotation. The compression was simulated by forcing a displacement (of 1 mm/min rate) from the top of the specimen to the bottom.

For accuracy reasons, quadrilateral elements CQUAD4 are generally preferred over the triangular elements CTRIA3, since the latter may exhibit excessive stiffness. However, the highly warped and curved gyroid surface made the CTRIA3 the most suitable element for the meshing process. A CQUAD4-CTRIA3 comparative study was performed on PLA cubic gyroids featuring different side sizes (1L, 2L, 3L, 4L, with L=10.5 mm). The same number of elements ($\approx$3500 per unit LxLxL cell) was used for the CQUAD4- and CTRIA3-based meshes. Although CQUAD4 elements led to a more accurate description of the non-linear behavior at compression, the CTRIA3 solution did not significantly differ from the CQUAD4 one. The variation of the Young modulus values did not exceed the 2.3% (LxLxL gyroid simulation), while the yield stress values the 4.5% (4Lx4Lx4L gyroid simulation). On the contrary the computational cost for the QUAD4 was up to 6 times higher than the CTRIA3.

5. Results and Discussion

5.1. Paraffin and Paraffin-based Blends

The DSC traces of the SasolWax 0907 loaded with 1 wt% CB (W1) and of the paraffin-SEBS-MA blends (S05W1, S10W1) are reported in the Fig. 6a and the relevant quantities are summarized in Table 4. The unblended paraffin formulation features melting onset temperature ($T_{on,m}$) at 47.4°C and a melting end temperature ($T_{end,m}$) at 110.7°C, with the (broad) melting trace exhibiting a minimum

29

peak value at 73.1°C. No solid-solid crystalline phase transition is observed for this composition, due to the microcrystalline nature of the SasolWax 0907. The $T_{on,m}$ and $T_{end,m}$ are not altered by the SEBS-MA addition. This evidence confirms the experimental findings from polyammide 12- SEBS-MA blends reported by Jose et al. [67]. In the DSC traces the paraffin-melting is the only observed phenomenon prior the marked endotherm due to the wax degradation captured by the TG (see Fig. 6b). Being amorphous (or semi-crystalline) the SEBS-MA shows no DSC endotherm due to the phase change. When moving from the W1 formulation to the SEBS-MA data, the thermal degradation onset temperature ($T_{on,deg}$) shows a monotonic increase for increasing copolymer content, as reported in Table 4. Similarly, the SEBS-MA-containing blends show increasing degradation end temperature ($T_{end,deg}$) as the copolymer mass fraction increases. This is related to the higher $T_{on,deg}$ and $T_{end,deg}$ of the SEBS-MA (419.5°C, and 462.4°C, respectively). In the temperature range 30 to 600°C, the W1-based formulations show a percent mass change (Δm_{30-600}) spanning from 91% to 97%, with increasing SEBS-MA content lowering the residual mass at high temperature (see Table 4). The SEBS-MA degradation is nearly completed at 600°C (see Fig. 6b, and Table 4), while the residual mass of the W1-based formulations is due to the presence of residuals in the microcrystalline wax (a result supported by the data discussed in Ref. [68]).

Compression tests were performed to determine the mechanical properties of paraffin blends and to quantify the strengthening effect of SEBS-MA on the W1 formulation. Results are reported in Table 5 and in Fig. 7 showing ensemble average curves (each defined by averaging four tests, and with error bars identified by standard deviation). Each average curve is traced as a solid line from the test start to the failure point, while a dashed line is used from the latter point on.

30
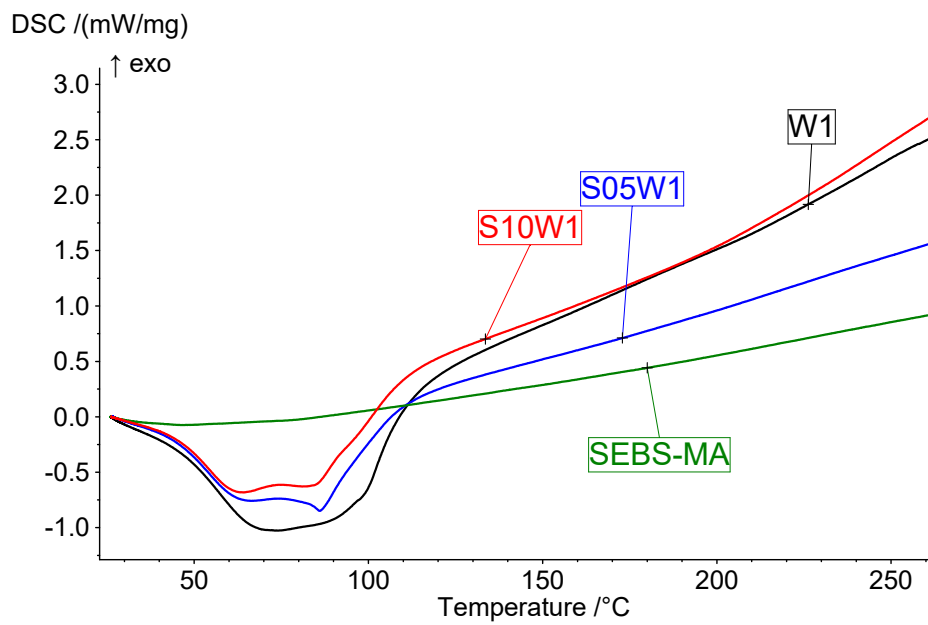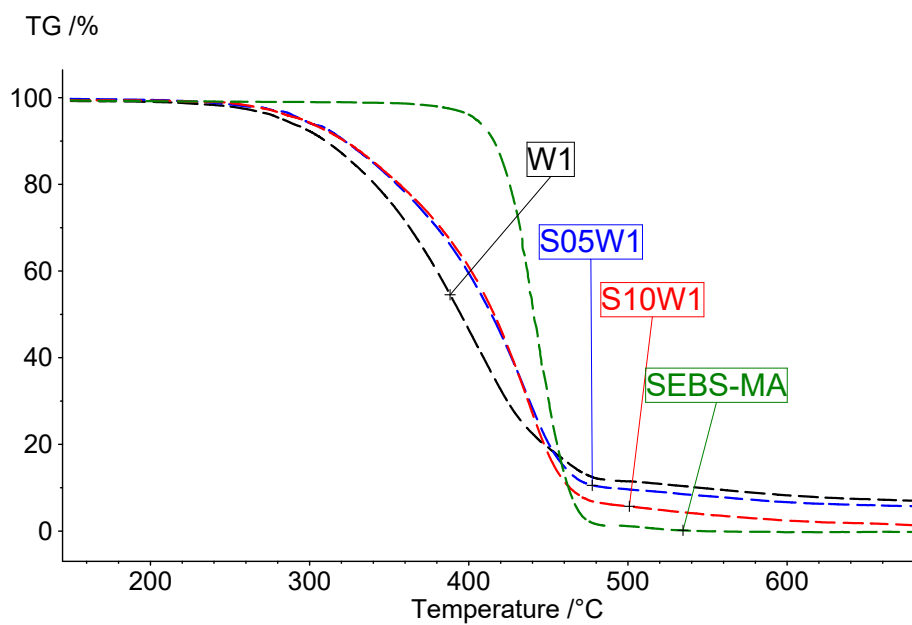
Figure 6: Slow heating rate behavior of W1 and paraffin-based SEBS-MA-containing blends: (a) DSC, detail in the range 30-250°C, (b) TG (10°C/min, 75 ml/min *Ar*, 10.0 ± 0.5 mg).

31

Table 4: TG-DSC data for paraffin-based fuels W1, S05W1, S10W1 and SEBS-MA (10°C/min, 75 ml/min *Ar*, 10.0 ± 0.5 mg).

Specimen	Melting Onset temperature, $T_{on,m}$ [°C]	Melting End temperature, $T_{end,m}$ [°C]	Degradation Onset temperature, $T_{on,deg}$ [°C]	Degradation End temperature, $T_{end,deg}$ [°C]	Mass change (30-600°C), Δm_{30-600} [%]
W1	47.4	110.7	326.0	448.8	-91.0
S05W1	45.6	111.7	362.2	459.7	-93.0
S10W1	46.0	111.6	372.3	460.4	-97.0
SEBS-MA	-	-	419.5	462.4	-99.6

All the investigated paraffin formulations experience a vertical columnar cracking after rupture. The W1 fuel shows a brittle behavior and the specimen rupture occurs after the yield point is reached, hence no plastic deformation is present. For this reason, the yield stress and the yield strain coincide with the ultimate compressive strength and the elongation at break, respectively. The mechanical properties of W1 reported in Table 5 are consistent with the previous studies on the SasolWax 0907 [41]. The blended formulations feature a stiffer and stronger compression behavior than W1, since their E and σ_y are increased, as shown in Fig. 7. The Young modulus is increased by 27% when passing from W1 to S05W1. Higher polymer mass fraction does not lead to further improvement, being E of the S10W1 similar to the one of the S05W1. The 5%-SEBS-MA addition does not alter the ϵ_y of the blend with respect to W1 (note the overlapped uncertainty interval in the Table 5 data). On the other hand, the σ_y of the S05W1 is increased of nearly 30%. The S10W1 exhibits σ_y and ϵ_y enhancements over the baseline of 42% and 26% respectively. Despite an increase of the compressive strength thanks to the SEBS-MA addition, the paraffin-based fuel blends still fea-

₅₃₁ ture a brittle failure characterized by the absence of a plastic field (see Fig. 7).

₅₃₂ After the yield point (or failure point), the sample, even if cracked, still exerts re-

₅₃₃ sistance to compression. It is noteworthy that the S05W1 blend features the most

₅₃₄ abrupt decrease of stress after rupture.

Table 5: Mechanical properties of paraffin-based fuel blends (compression rate 1 mm/min, testing temperature 25 ± 5 °C).

Specimen	Young modulus, E [MPa]	Yield stress, σ_y [MPa]	Yield strain, ϵ_y [%]
W1	407 ± 18	3.46 ± 0.13	1.47 ± 0.05
S05W1	519 ± 30	4.46 ± 0.15	1.34 ± 0.15
S10W1	510 ± 15	4.92 ± 0.29	1.86 ± 0.05

₅₃₅ *5.2. 3D Printer Materials*

₅₃₆ The investigation of the characteristics of the 3D printer materials focused on

₅₃₇ their thermal, mechanical and wettability behaviors. Relevant data for the thermal

₅₃₈ characterization of the FDM filaments are reported in the Table 6. The observable

₅₃₉ parameters of interest include the glass transition temperature (T_g), a second order

₅₄₀ effect [69]. The analysis highlights the amorphous nature of ABS testified by the

₅₄₁ absence of a melting endotherm. All the polymers feature a glass transition tem-

₅₄₂ perature in the investigated T range. The evaluation of $T_{on,deg}$ and $T_{end,deg}$ suggests

₅₄₃ that NY is the most stable material from the thermal point of view. Polylactic acid

₅₄₄ is the tested polymer exhibiting the lowest $T_{on,deg}$. In particular, the $T_{on,deg}$ differ-

₅₄₅ ence between PLA and W1 is limited to 20°C (Table 4). Moreover, the $T_{end,deg}$

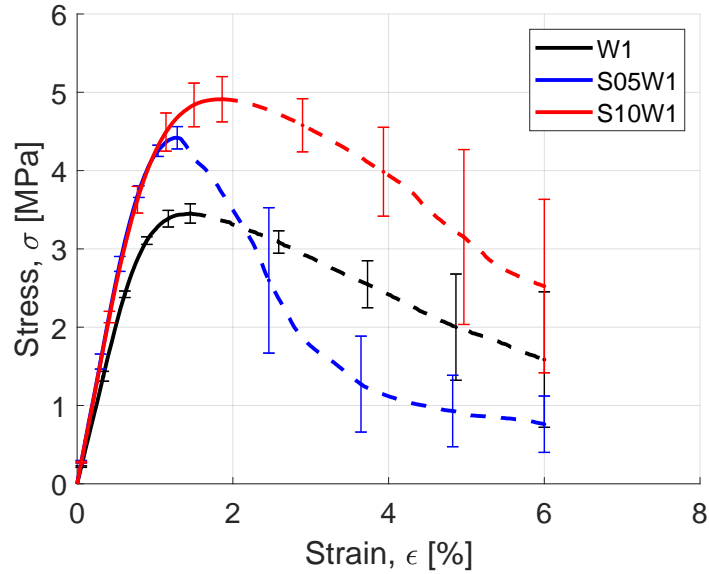₅₄₆ of PLA is 70°C lower than the one of W1. Nylon exhibits the highest $T_{end,deg}$,

33

Figure 7: Engineering stress-strain curves of paraffin-based formulations (ensemble average curves, compression rate 1 mm/min, testing temperature 25 ± 5 °C).

but this value does not exceed the 25°C difference with respect to the W1 fuel. These results suggest the suitability of the selected materials for the realization of the structure strengthening the fuel grain. During the combustion process the paraffin fuel regresses due to vaporization and entrainment. The degradation temperature of the reinforcing structure occurs in the same temperature range as the paraffin degradation/vaporization. During burning, the gyroid structure will probably pyrolyze but offering the presence of elements providing a slower regression than the paraffin. These elements could provide an helpful reinforcement of the burning grain while granting the creation of recirculating zones improving the convective heat transfer and thus, the r_f. Such a (likely) behavior has been confirmed by preliminary studies [70], but the ballistic assessment requires dedicated investigations that are beyond the scope of this work.

34

Table 6: TG-DSC data for FDM polymers for gyroid printing (10°C/min, 75 ml/min Ar, 10.0 ± 0.5 mg).

Specimen	Glass transition temperature, T_g [°C]	Melting Onset temperature, $T_{on,m}$ [°C]	Melting End temperature, $T_{end,m}$ [°C]	Degradation Onset temperature, $T_{on,deg}$ [°C]	Degradation End temperature, $T_{end,deg}$ [°C]
PLA	61.6	144.4	158.5	346.7	378.9
ABS	109.2	-	-	374.9	452.0
NY	56.6	178.2	199.8	423.0	471.6

The gyroid structure embedded in the paraffin fuel grain is aimed at providing mechanical strength. The achievement of this goal requires a material with suitable characteristics in terms of both mechanical behavior and paraffin wetting. The critical surface tension results for PLA, ABS and NY are reported in Table 7. Figure 8 shows the contact angle values of different polymer - testing liquid couples. Each testing liquid is characterized by its own surface tension (γ_L). The linear fitting relating $\cos(\theta)$ and the γ_L is depicted in Fig. 8 and reported in Table 7. Polymers are low-energy surfaces and the critical tensions for the three investigated materials are close to each other. The data scattering limits the considerations on the (minor) differences in the average results. Armored grains are produced by melt casting. Thus, a critical role is played by the W1 surface tension under the casting condition. Open literature data report a SasolWax 0907 surface tension of 28 mN/m at 100°C [47]. The latter temperature is compatible with the casting condition of the armored grains. Considering the data reported in Table 7, $\gamma_{CR} > 28$ mN/m, hence a good wetting of the polymer surfaces is likely when pouring the melted paraffin. The surface texture of the reinforcing structure may play a role when coupling the gyroid with the melted paraffin. In particular,

surface roughness could obstacle the reinforcing structure wetting by paraffin. No detailed analysis of this aspect could be performed in this work. Further assessments of the surface roughness effects will be pursued in future investigations.

The melt casting for the armored grain manufacturing deserves an additional consideration. During this process, the temperature of the melted paraffin wax is approximately 100°C, a value that could lead to the softening of the polymers used for the gyroids. In particular, the glass transition temperature of PLA and NY is below 100°C (refer to Table 6). However, the softening point of a polymer is captured by the heat deflection temperature (HDT) rather than the T_g. In fact, the HDT gives an indication of how the material behaves when stressed at high temperatures. The heat deflection temperatures of PLA and ABS for the filaments used in the current study are 55°C (at 0.45 MPa) [71] and 101°C (at 1.8 MPa) [72]. From accessible data, the HDT of the NY filament is ≈93°C (at 1.8 MPa) [73]. These values suggest that PLA is the most problematic material and that it could be softened during the grain manufacturing, especially if external pressure is applied to contrast the paraffin shrinkage. On the contrary, ABS and NY should be less prone to this phenomenon. The possible softening of the gyroid during the manufacturing of the armored grain is a concern that deserves further studies, especially in large grains. In the current study, the pouring of melted paraffin during the manufacturing process did not seem to jeopardize the gyroid structure, regardless the polymer used. It is worth noting that PLA could be of interest as a gyroid-printing polymer when low melting point paraffin waxes are considered, since their casting temperatures would be reduced with respect to the SasolWax 0907.

Mechanical properties under compression of the bulk materials are reported

36

Table 7: Cosine of the contact angle as a function of the γ_L, linear fitting of the experimental points and γ_{CR} for the investigated reinforcing structure polymers.

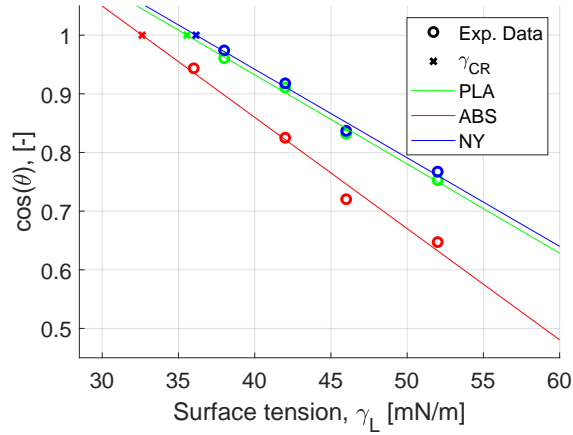| Specimen	Critical surface tension, γ_{CR} [mN/m]	Linear fitting, $\cos(\theta) = A \cdot \gamma_L + B$	R^2
PLA	35.6 ± 1.8	-0.015 γ_L +1.541	0.993
ABS	32.6 ± 3.1	-0.019 γ_L +1.619	0.981
NY	36.2 ± 2.3	-0.015 γ_L +1.546	0.988

Figure 8: Cosine of the contact angle as a function of the γ_L for the reinforcing structure polymers, and linear fitting of the experimental data: γ_{CR} corresponds to $\cos(\theta) = 1$. Error bars are not reported for the sake of readability.

601 in Table 8. The compression stress-strain curves of the three investigated poly-
602 mers are shown in Fig. 9. A post-yield softening can be appreciated for the PLA
603 specimens, while this trend is not encountered in ABS and NY samples. Com-
604 pared to PLA, ABS exhibits lower Young modulus (-47%) and yield stress (-34%).
605 However, ABS features a higher yield strain than PLA (+50%) and a nearly con-

37

stant post-yield stress. Under the investigated conditions, NY absorbs a moderate

deformation energy and it is characterized by a strain hardening (Fig. 9). This

behavior complicates the identification of the yield point, according to ISO 604

standard [56]. Due to this, NY data reported in Table 8 are evaluated adopting a

method defined by the ISO 13314 [74]. In particular, the yield point of the material

is identified as the one producing an offset strain of 0.2%. Data in Table 8 include

two densities: the bulk density and the theoretical maximum density (TMD). The

former is defined as the ratio between the specimen mass and the actual volume,

while the latter coincides with the density of the polymeric filament. The bulk

density values always result lower than the TMDs for all the investigated poly-

mers. This evidences the creation of some voids inside the printed object during

the FDM process.

Table 8: Mechanical properties of the 3D printer materials (100% *concentric* infill, compression rate 1 mm/min, testing temperature 25 ± 5 °C).

Specimen	Young modulus, E [MPa]	Yield stress, σ_y [MPa]	Yield strain, ϵ_y [%]	Bulk density, ρ_{bulk} [g/cm^3]	TMD, ρ_{TMD} [g/cm^3]
PLA	2349 ± 64	68.48 ± 2.54	4.34 ± 0.20	1.20 ± 0.01	1.26 ± 0.00[a]
ABS	1243 ± 12	44.88 ± 0.48	6.53 ± 0.19	1.05 ± 0.01	1.08 ± 0.00[a]
NY[b]	1409 ± 45	45.62 ± 0.80	3.44 ± 0.16	1.04 ± 0.01	1.13 ± 0.00[a]

[a] Over three measurements, the confidence interval is < 0.001.

[b] Data reduction follows ISO 13314 standard [74] instead of ISO 604 [56].

5.3. Gyroid Structure Behavior

The mechanical assessment of the empty gyroid structures was performed by

means of compression tests and FEA. The experimental compression tests fo-

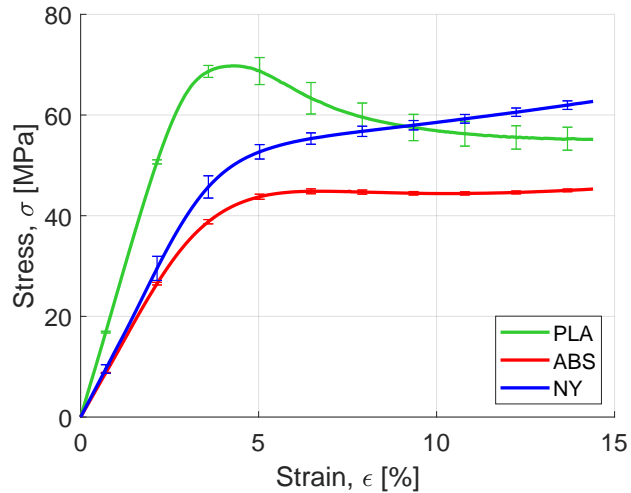cused on gyroids printed in PLA featuring three $\tilde{\rho}_\%$ (7%, 10%, 15%). For the sake

Figure 9: Engineering stress-strain curves of PLA, ABS, NY (ensemble average curves, compression rate 1 mm/min, testing temperature 25 ± 5 °C).

of completeness, the tested gyroids were produced following both the *infill* and *SPLab* methods. The results of the mechanical tests are shown in Table 9 collecting *infill* (I-PLA_iXX) and *SPLab* (S-PLA_iXX) gyroids. Data show enhanced mechanical properties (stiffness, strength, and elastic limit) for increasing relative densities (or infill) for both the gyroid manufacturing methods. Considering the gyroids with the same nominal infill, a good agreement is observed between the I- and the S-series. However, the yield strain of I-PLA_i15 differs from the one of S-PLA_i15. The reason for the high yield strain of S-PLA_i15 is that its stress-strain curve features a strain hardening and the curve does not experience a drop after the elastic limit, as depicted in Fig. 10. It should be also pointed out that the actual relative densities of *infill gyroids* and *SPLab gyroids* are slightly different. In fact, different gyroid production techniques affect the printing process (see Fig. 4).

39

Finite element analysis was conducted to simulate the mechanical behavior of the gyroids during compression. The numerical investigation was performed considering all the three different 3D printer materials (PLA, ABS and NY). The mechanical properties resulting from the simulations are reported in Table 10. The FEA results for PLA_i07 are shown in Fig. 11. The results of Table 10 highlight the effect of the bulk material in the definition of the gyroid mechanical properties. Considering gyroids featuring the same relative density but different materials, PLA lattices result stiffer and characterized by higher compressive yield stress than the ABS and NY counterparts. This trend is consistent with the mechanical behavior of the bulk polymers reported in Table 8. Numerical results also underlines the importance of the relative density $\tilde{\rho}_\%$, regardless the material the gyroids are made of: the higher relative density, the higher mechanical properties. This result captures and confirms experimental evidences from compression tests (see Table 9).

Comparing data for the PLA gyroids in Table 10 with the experimental results in Table 9, it is evident that the FEA overestimates the mechanical properties of the real structures. Finite element analysis does not take into account the presence of printing defects during the gyroid manufacturing as layer-to-layer adhesion or the presence of saddles due to the discrete height difference during the extrusion of following layers (shown in Fig. 4). This is reflected into a gap between the actual and the numerical behavior under compression of the structures. In addition to this, differences between actual and FEA data is related to the mass discrepancy between the manufactured gyroids and their simulated counterparts. In fact, although the geometry is the same for all the investigated gyroids, the I-series is characterized by open saddle points, that are lessened in the case of the *SPLab*

40

gyroids. Conversely, FEA gyroids do not feature saddles and exhibit higher mass

(and thus, higher lattice density) than the I- and S-series gyroids (see Table 9).

Table 9: Mechanical properties of PLA-gyroids realized by the *infill gyroid* (I-PLA_iXX) and *SPLab gyroids* (S-PLA_iXX) technique (compression rate 1 mm/min, testing temperature 25 ± 5 °C).

Specimen	Young modulus, E [MPa]	Yield stress, σ_y [MPa]	Yield strain, ϵ_y [%]	Lattice density, ρ [g/cm^3]	Relative density, $\tilde{\rho}_\%$ [%]
I-PLA_i07	31 ± 2	0.69 ± 0.06	2.53 ± 0.23	0.09 ± 0.00[a]	7.8 ± 0.1
I-PLA_i10	60 ± 3	1.50 ± 0.04	3.11 ± 0.08	0.12 ± 0.00[a]	10.2 ± 0.1
I-PLA_i15	109 ± 1	2.96 ± 0.01	3.89 ± 0.12	0.18 ± 0.00[a]	14.6 ± 0.1
S-PLA_i07	36 ± 3	0.81 ± 0.07	2.72 ± 0.14	0.10 ± 0.00[a]	8.4 ± 0.1
S-PLA_i10	66 ± 2	1.87 ± 0.12	3.36 ± 0.34	0.14 ± 0.00[a]	11.8 ± 0.1
S-PLA_i15	88 ± 4	3.09 ± 0.05	6.15 ± 0.64	0.21 ± 0.00[a]	17.5 ± 0.1

[a] Over three measurements, the confidence interval is < 0.01.

Table 10: Mechanical properties of FEA simulated gyroids.

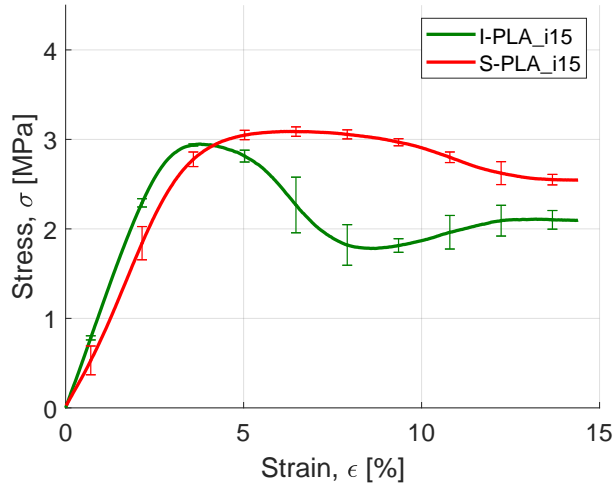| Specimen	Young modulus, E [MPa]	Yield stress, σ_y [MPa]	Yield strain, ϵ_y [%]	Lattice density, ρ [g/cm^3]	Relative density, $\tilde{\rho}_\%$ [%]
PLA_i07	49	1.42	3.79	0.11	8.9
PLA_i10	85	2.72	3.84	0.15	13.0
PLA_i15	146	4.13	3.02	0.23	19.8
ABS_i07	25	0.82	4.23	0.09	8.9
ABS_i10	44	1.65	4.58	0.14	13.0
ABS_i15	75	2.31	3.27	0.21	19.8
NY_i07	29	0.99	4.46	0.09	8.9
NY_i10	50	2.05	5.00	0.13	13.0
NY_i15	86	2.81	3.44	0.20	19.8

Figure 10: Engineering stress-strain curves of I-PLA_i15 and S-PLA_i15 (ensemble average curves, compression rate 1 mm/min, testing temperature 25 ± 5 °C).
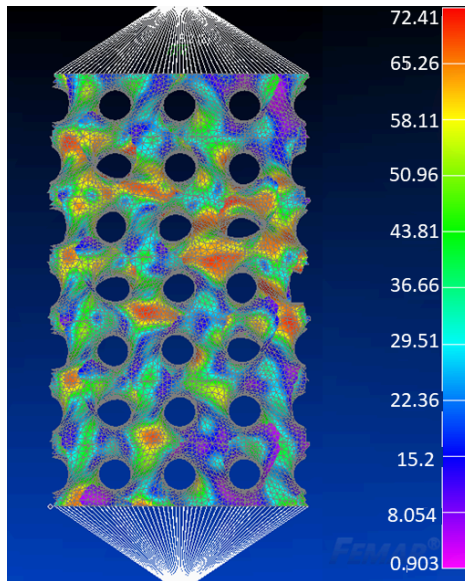

Figure 11: Von Mises stresses (in MPa) from FEA for the PLA_i07 gyroid (4.2% strain).

Experimental test campaign and numerical simulations highlight that higher $\tilde{\rho}$ results in better mechanical properties. According to Ref. [19], the $E(\tilde{\rho})$ can be written as:

$$\frac{E}{E_{\text{bulk}}} = a_E \cdot \tilde{\rho}^{\,n_E} \tag{8}$$

For what concerns the yield stress, the $\sigma_{\text{y}}(\tilde{\rho})$ is captured by:

$$\frac{\sigma_{\text{y}}}{E_{\text{bulk}}} = a_\sigma \cdot \tilde{\rho}^{\,n_\sigma} \tag{9}$$

The application of Eqs. (8) and (9) requires the Young modulus (E_{bulk}) of the bulk materials (Table 8). The $E(\tilde{\rho})$ and $\sigma_{\text{y}}(\tilde{\rho})$ resulting from the compression tests are reported in Fig. 12, while power law interpolations for Eqs. (8) and (9) are shown in Tables 11 and 12. The experimental fitting curves match quite well the *infill gyroids* and *SPLab gyroids* data for both the Young modulus (Fig. 12a) and the yield stress (Fig. 12b). Concerning the Young modulus fitting curves, Fig. 12a and Table 11 suggest a matching between experimental and numerical results. A slightly lower data fitting characterizes $\sigma_{\text{y}}(\tilde{\rho})$ fitting of Fig. 12b, as testified by the data reported in Table 12. Table 11 and Table 12 also include the coefficients predicted by Ashby [19]. Focusing on PLA gyroids, coefficients a_E and n_E are the same for both the experimental and numerical results. The values of the exponential factor n_E confirm that gyroid lattice deforms in a bending-dominated manner. In general, the coefficients of $\sigma_{\text{y}}(\tilde{\rho})$ scaling law (Table 12) are more scattered than those of $E(\tilde{\rho})$ scaling law (Table 11). However, good agreement between experimental and numerical results is achieved. Table 11 evidences that FEA fitting coefficients are not influenced by the material, suggesting that the scaling law is valid regardless the material the gyroid is made of. The same consideration holds for the $\sigma_{\text{y}}(\tilde{\rho})$

43

scaling law (Table 12).

(a) $E(\tilde{\rho})/E_{\text{bulk}}$ fitting Eq. (8).

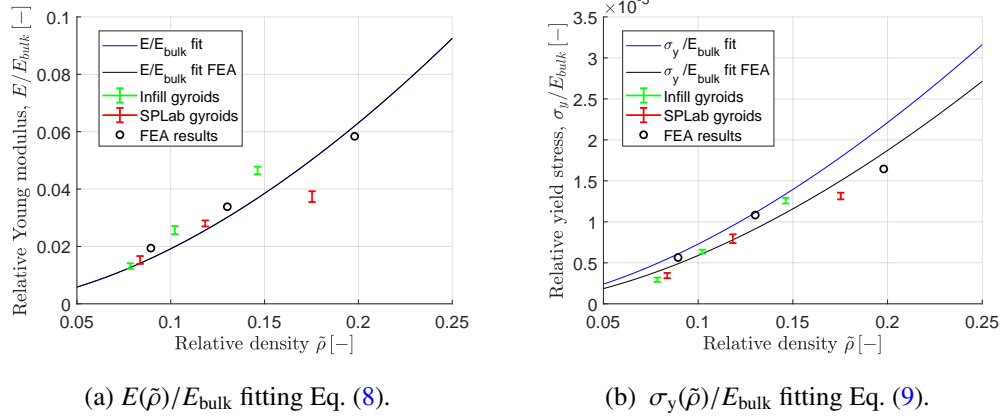(b) $\sigma_{\text{y}}(\tilde{\rho})/E_{\text{bulk}}$ fitting Eq. (9).

Figure 12: Scaling laws for gyroids produced in PLA, fitting of experimental and numerical results.

Table 11: $E(\tilde{\rho})/E_{\text{bulk}}$ fitting [Eq. (8)] for experimental and FEA gyroids. Uncertainties are evaluated by 95% confidence level.

	a_E	n_E	R^2
Ashby [19] **bending-dominated**	1	2	-
Ashby [19] **stretching-dominated**	1	1	-
PLA gyroids, exp.	1.00 ± 0.02	1.72 ± 0.14	0.9996
PLA gyroids, FEA	1.00 ± 0.02	1.72 ± 0.16	0.9999
ABS gyroids, FEA	1.00 ± 0.02	1.72 ± 0.16	0.9999
NY gyroids, FEA	1.00 ± 0.02	1.72 ± 0.15	0.9999

Table 12: $\sigma_y(\tilde{\rho})/E_{\text{bulk}}$ fitting [Eq. (9)] for experimental and FEA gyroids. Uncertainties are evaluated by 95% confidence level.

	a_σ	n_σ	R^2
Ashby [19]	0.05	2	-
PLA gyroids, exp.	0.029 ± 0.000	1.60 ± 0.13	0.9994
PLA gyroids, FEA	0.027 ± 0.001	1.67 ± 0.22	0.9998
ABS gyroids, FEA	0.034 ± 0.002	1.72 ± 0.30	0.9997
NY gyroids, FEA	0.040 ± 0.002	1.78 ± 0.34	0.9997

5.4. Armored Grains

The gyroids embedded in the armored grains were printed according to the *infill gyroid*. This choice was based on the similar mechanical behavior of *infill* and *SPLab gyroids* featuring the same nominal infill percentage (as shown in Table 9), and the longer printing time required by the *SPLab gyroids*.

Due to the heterogeneous structure of the armored grain, its compression behavior is influenced by the reinforcing structure-paraffin wax adhesion. The experimental results summarized in Table 7 suggest a good wetting of the printed polymer by the melted paraffin. This is a necessary conditions for good adhesion, since better wetting can increase the adhesive bond strength. The adhesion between the gyroid structure and the paraffin was studied by measuring the materials surface free energy [Eqs. (5)-(6)] and the reversible ideal work between W1 and each polymer [Eq. (7)]. The results are reported in Table 13. The surface free energy of polymers is mainly affected by the dispersion component. Among all the polymers, the one that features the highest polar component is the PLA. On

the contrary, the polar contribution in W1 paraffin can be considered negligible. The W_a provides a grade of the paraffin-gyroid coupling (i.e., the higher the work of adhesion, the larger the energy per unit area required to reversibly separate the paraffin from the reinforcing structure). Under the investigated conditions, the W_a shows similar values for all the reinforcing materials used for the gyroid printing. Hence, no significant difference between the polymers can be appreciated. From the adhesion point of view, all the three polymers are suitable to be the 3D printer material for the gyroid, and there is no a preferable material.

Table 13: Surface free energy of the investigated reinforcing materials and paraffin-polymer work of adhesion.

Specimen	Surface free energy = polar + dispersion $\gamma = \gamma^p + \gamma^d$ [mJ/m²]	Work of adhesion W1-polymer, W_a [mJ/m²]
W1	37.7 = 0.4 + 37.3	-
PLA	52.2 = 15.4 + 36.8	79.0
ABS	46.9 = 9.9 + 37.0	78.3
NY	46.8 = 10.4 + 36.4	77.8

For the armored grains, the effects of the gyroid infill on the mechanical properties are investigated for PLA at 7%, 10%, and 15% infill. The same reinforcing structure is used for ABS and NY for the 15% infill. The Fig. 13 shows a typical compression test. During the specimen compression, the structure helps the paraffin improving the strength of the material that forms slivers, but it does not crack in a frail way. Such behavior was attested for all the armored grains, regardless the polymer used for the reinforcing gyroid. Ensemble average $\sigma(\epsilon)$ curves

for the armored grains are reported in Fig. 14, emphasizing the effect of the infill percentage and of the gyroid material. Figures 14a and 14b show the ductility achieved by armored grains thanks to the gyroid reinforcing structures. The comparison between the armored grains mechanical properties and the W1 baseline is reported in Table 14. The W1 formulation features a mechanical response to the compression characterized by a brittle behavior, with failure occurrence after the yield point (σ_y= 3.46 MPa, ϵ_y= 1.47%). While W1 features a significant post-yield stress decrease, the addition of the PLA gyroids stops this decay to a plateau value (Fig. 14a). The W1_ABS_i15 and W1_NY_i15 exhibit a similar mechanical behavior with a plastic field for $\sigma > \sigma_y$ (Fig. 14b). Table 14 clearly shows that the paraffin-SEBS-MA blends feature higher σ_y than the W1, while the ϵ_y is slightly changed. Moreover, the yield point coincides with the failure point for paraffin-based blends, while it marks the boundary between the elastic and the plastic regions for the armored grains. The brittle behavior of paraffin formulations and the ductile of armored grains is confirmed by comparing Fig. 7 and Fig. 14. This evidence is suggested by the width of the error bars and the stress drop after the yield point.

For what concerns the PLA gyroids in Fig. 14a, the Young modulus is not significantly altered by the infill percentage of the embedded structure. Although the W1_PLA_i07 and the W1_PLA_i15 show a 10% decrease and a 10% increase over the W1 baseline, respectively, the overlapping error bars limit the considerations on the positive influence of higher infills. On the contrary, the compressive yield stress increases monotonically by the presence of denser reinforcing structures. This result is in agreement with the mechanical behavior of PLA gyroids in Table 9. In fact, higher infill of the gyroids significantly enhanced the σ_y and

47

ϵ_y. Similarly, the armored grains embedding denser gyroids show higher structural properties (in particular, at yield). The best results are achieved by the 15% infill: W1_PLA_i15 offers σ_y and ϵ_y increases over the W1 of 64% and a 132%, respectively. The W1_ABS_i15 shows a nearly negligible σ_y increase over W1, with a 20% reduction in E. While the E reduction is not critical (per se), the armored grain shows a 213% increase in ϵ_y with respect to the W1 thanks to the ABS gyroid. The mechanical performance enhancement of W1_NY_i15 reaches 35% when considering σ_y, and 296% for ϵ_y. For the NY-reinforced armored grain, these attractive results are afforded at the expense of a faint E reduction (see Table 14). Figure 14b highlights that the armored grains mechanical properties are related to the material used for the reinforcing gyroid. The trends of the armored grains follow qualitatively those of the raw materials shown in Fig. 9. The W1_PLA_i15 is the specimen with the highest σ_y and with the post-yield softening, the W1_ABS_i15 features the lowest plateau stress, and the W1_NY_i15 exhibits the largest ϵ_y and the highest plateau stress. Similarly, the PLA is the stiffest material, the ABS is the lowest rigid polymer, while the NY is though and characterized by a strain hardening (Fig. 9). From the mechanical point of view, the NY seems to be the most attractive material for the armored grain, because of the higher σ_y and ϵ_y with respect to the W1 baseline and of its toughness, making the armored grain capable of absorbing energy during the deformation.

6. Conclusions and Future Developments

The armored grain, a paraffin grain embedding a 3D printed cellular structure for mechanical properties reinforcement, was investigated and proposed as a solu-
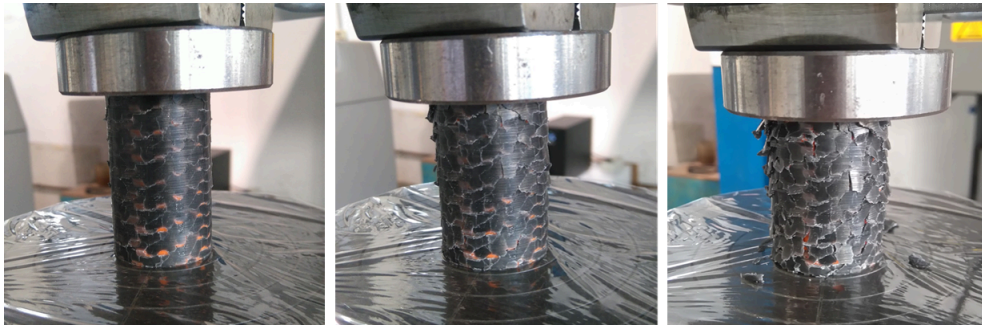
48

Figure 13: Pictures of W1_ABS_i15 during the compression test.

Table 14:   Comparison between mechanical properties of paraffin-based blends and of armored grains with respect to the W1 paraffin baseline.

Specimen	Young modulus, E [MPa]	Yield stress, σ_y [MPa]	Yield strain, ϵ_y [%]
W1	407	3.46	1.47
S05W1	+ 27.4%	+ 28.9%	- 9.3%
S10W1	+ 25.3%	+ 42.2%	+ 26.2%
W1_PLA_i07	- 10.2%	+ 2.6%	+ 17.2%
W1_PLA_i10	+ 3.2%	+ 14.3%	+ 56.1%
W1_PLA_i15	+ 9.9%	+ 64.0%	+ 132%
W1_ABS_i15	- 19.6%	+ 1.8%	+ 213%
W1_NY_i15	- 4.9%	+ 34.9%	+ 296%

tion to cope with the fragility of alkane waxes. The selected cellular structure was the gyroid, a triply periodic minimal surface that can be easily 3D printed. A complete pre-burning and mechanical characterization of the armored grain was per-
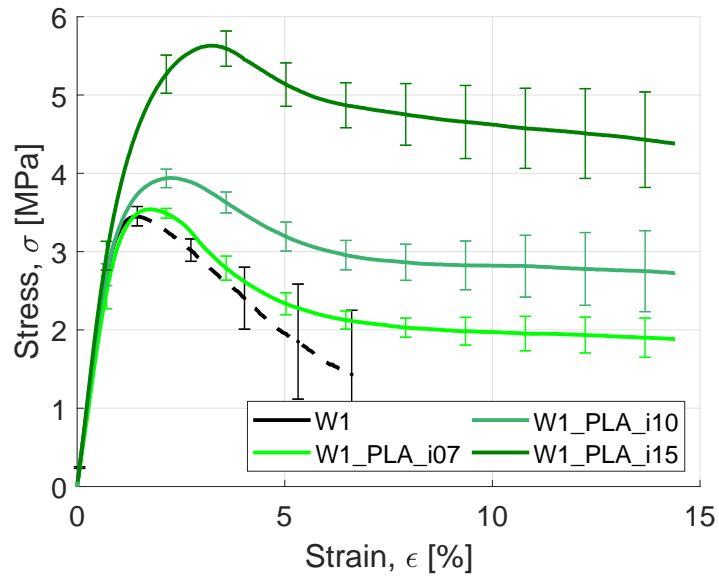
(a) PLA-based armored grains.
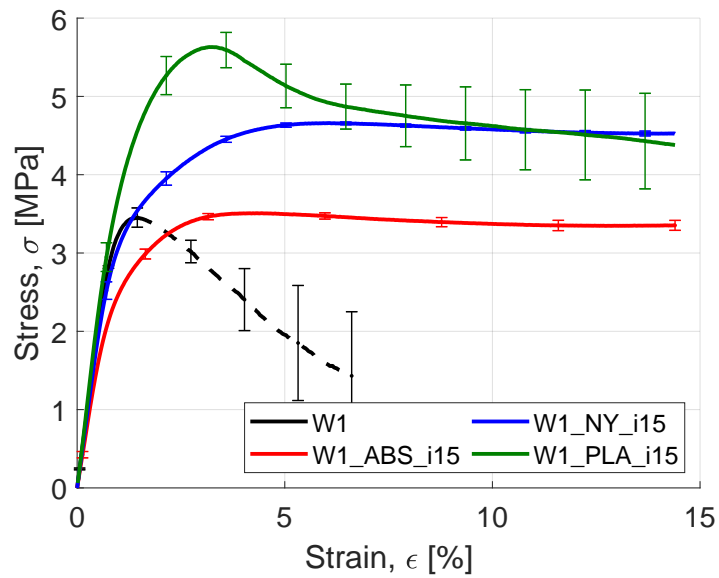
(b) 15% infill armored grains.

Figure 14: Engineering stress-strain curves of armored grains (ensemble average curves, compression rate 1 mm/min, testing temperature 25 ± 5 °C).

formed. Three different materials were employed for the gyroid structure: poly-lactic acid (PLA), acrylonitrile-butadiene-styrene (ABS) and nylon 6 (NY). The mechanical properties and the thermal behavior of the bulk materials were studied by means of compression tests and simultaneous thermal analyses (TG/DSC). Materials compatibility investigation was performed to understand if the different polymer-paraffin couples could satisfy the wetting and adhesion criteria. All the investigated materials show suitable characteristics as embedded reinforcing structures. The 3D printer materials featured critical surface tensions higher than the surface tension of the melt paraffin during the melt casting procedure.

The mechanical response of the gyroid was investigated by compression tests using PLA and reinforcing structures printed with different infills (7%, 10%, and 15%). The compressive yield stress and strain are monotonically enhanced by the presence of denser lattices. Finite element analysis (FEA) was used to develop models of PLA gyroid structures. These, in turn, enabled an evaluation of the achieved overall print quality. Although the FEA results overestimated the actual mechanical properties, the simulation results are comparable with the experimental values. The achieved results were useful to understand the mechanical properties of the gyroids and to capture their scaling laws. The FEA results suggested the independence of the scaling laws from the material the gyroid is produced by. Therefore, once scaling laws are derived, they could be applicable to any material to predict the mechanical properties of a generic gyroid characterized by a specific relative density. Scaling laws suggested a bending-dominated behavior for the gyroid.

Finally, the effectiveness of the armored grain for the reinforcement of paraffin fuels was assessed. Armored grains featuring different gyroid structures and

materials (PLA, ABS, NY) were studied via compression tests. The insertion of a gyroid reinforcing structure in the paraffin actually affects the mechanical properties. The Young modulus of armored grains is generally lower, or at least of the same order, than that of pure paraffin. Hence, the reinforcing structure does not significantly affect the stiffness of the pristine paraffin wax. This is not considered a critical issue, being fragility the critical point of paraffin waxes. The yield stress augments with the relative density $\tilde{\rho}$ (i.e., percent infill) enhancement and depends on the printed material. The same applies for the yield strain. Further numerical investigations will be performed to predict the armored grain behavior as a function of $\tilde{\rho}$ and the raw materials (paraffin and polymer used for the gyroid). The relevant outcome of the investigation is that the fragile behavior of the pristine paraffin wax is turned in a ductile behavior of the armored grain. This result is of breakthrough relevance. With pure paraffin as baseline, the armored grains with gyroids printed at 15% infill feature a strain at yield increase ranging from 132% for PLA to 296% for NY. Thus, the armored grains outperform the conventional reinforcing strategy of blending considered in the analysis. Fuels in which the paraffin wax is blended with a styrene-ethylene-buthylene-styrene copolymer grafted with maleic anhydride provide similar yield stress increases, though the corresponding strain is lower than that achieved by the armored grains with 15% infill. Moreover, two further points should be considered. First, for the blended formulations the mechanical behavior is still fragile, with the specimen yield point coinciding with its failure. Second, blending affords mechanical properties buying this performance by increased melt layer viscosity and, thus, regression rate reduction. Although the ballistic response of the armored grain requires future investigations, the wide availability of paraffin suggests the possibility to achieve

fast regression rates. Considering the armored grain results, the NY reveals to be the most appealing material, albeit all the 3D printer polymers lead to a structural improvement.

The attractive mechanical properties revealed by the investigation of the armored grain offer the opportunity of a significant impact on the development of high-performing green paraffin-based fuels. The achieved results suggest to focus the future experimental steps on a detailed assessment of the regression rate behavior of armored grains to investigate infill and reinforcing material effects on the ballistic response of the fuel. Moreover, while the gyroid has shown interesting performance from the mechanical reinforcement, the analysis of different cellular structures should be pursued from both structural and combustion point of views.

References

[1] D. Altman, Overview and history of hybrid rocket propulsion, in: M. J. Chiaverini, K. K. Kuo (Eds.), Fundamentals of Hybrid Rocket Combustion and Propulsion, AIAA, 2007, Ch. 1, pp. 1–36. doi:https://doi.org/10.2514/5.9781600866876.0001.0036.

[2] A. Mazzetti, L. Merotto, G. Pinarello, Paraffin-based hybrid rocket engines applications: A review and a market perspective, Acta Astronaut. 126 (2016) 286–297. doi:https://doi.org/10.1016/j.actaastro.2016.04.036.

[3] G. Marxman, M. Gilbert, Turbulent boundary layer combustion in the hybrid rocket, Symp. (Int.) Combust. 9 (1) (1963) 371–383. `doi:https://doi.org/10.1016/S0082-0784(63)80046-6`.

[4] G. A. Marxman, C. E. Wooldridge, R. J. Muzzy, Fundamentals of hybrid boundary-layer combustion, Prog. Astronaut. Rocket. 15 (1964) 485–522. `doi:https://doi.org/10.1016/B978-1-4832-2730-6.50025-7`.

[5] G. A. Marxman, Combustion in the turbulent boundary layer on a vaporizing surface, Symp. (Int.) Combust. 10 (1) (1965) 1337–1349. `doi:https://doi.org/10.1016/S0082-0784(65)80268-5`.

[6] D. Pastrone, Approaches to low fuel regression rate in hybrid rocket engines, Int. J. Aerosp. Eng. 2012 (649753) (2012) 1–12. `doi:https://doi.org/10.1155/2012/649753`.

[7] M. J. Chiaverini, Review of solid-fuel regression rate behavior in classical and nonclassical hybrid rocket motors, in: M. J. Chiaverini, K. K. Kuo (Eds.), Fundamentals of Hybrid Rocket Combustion and Propulsion, AIAA, 2007, Ch. 2, pp. 37–126. `doi:https://doi.org/10.2514/5.9781600866876.0037.0126`.

[8] M. A. Karabeyoglu, D. Altman, B. J. Cantwell, Combustion of liquefying hybrid propellants: Part 1, general theory, J. Propul. Power 18 (3) (2002) 610–620. `doi:https://doi.org/10.2514/2.5975`.

[9] M. A. Karabeyoglu, B. J. Cantwell, Combustion of liquefying hybrid propellants: Part 2, stability of liquid films, J. Propul. Power 18 (3) (2002) 621–630. `doi:https://doi.org/10.2514/2.5976`.

[10] J. Noel, Solid propellant grain structural integrity analysis, Tech. Rep. NASA SP-8073, NASA Space Vehicle Design Criteria, Cleveland, OH (June 1973).

[11] S. Kilic, M. A. Karabeyoglu, J. Stevens, B. J. Cantwell, Modeling the slump characteristics of the hydrocarbon-based hybrid rocket fuels, in: 39th AIAA/ASME/SAE/ASEE Jt. Propuls. Conf. Exhib., Huntsville, AL, 2003, pp. 1–22. doi:https://doi.org/10.2514/6.2003-4461.

[12] M. A. Karabeyoglu, G. Zilliac, B. J. Cantwell, S. DeZilwa, P. Castellucci, Scale-up tests of high regression rate paraffin-based hybrid rocket fuels, J. Propul. Power 20 (6) (2004) 1037–1045. doi:https://doi.org/10.2514/1.3340.

[13] S. Sisi, A. Gany, Combustion of plain and reinforced paraffin with nitrous oxide, Int. J. Energ. Mater. Chem. Propul. 14 (4) (2015) 331–345. doi:https://doi.org/10.1615/IntJEnergeticMaterialsChemProp.2015011139.

[14] J. C. Thomas, J. M. Stahl, A. J. Tykol, F. A. Rodriguez, E. L. Petersen, Hybrid rocket studies using HTPB/paraffin fuel blends in gaseous oxygen flow, in: 7th Eur. Conf. for Aeronaut. and Space Sci. (EUCASS), Milan, IT, 2017, pp. 1–13. doi:https://doi.org/10.13009/EUCASS2017-251.

[15] S. Maruyama, T. Ishiguro, K. Shinohara, I. Nakagawa, Study on mechanical characteristic of paraffin-based fuel, in: 47th AIAA/ASME/SAE/ASEE Jt. Propuls. Conf. Exhib., San Diego, CA, 2011, pp. 1–9. doi:https://doi.org/10.2514/6.2011-5678.

[16] C. Paravan, L. Galfetti, F. Maggi, A critical analysis of paraffin-based fuel formulations for hybrid rocket propulsion, in: 53rd AIAA/SAE/ASEE Jt. Propuls. Conf., Atlanta, GA, 2017, pp. 1–17. doi:https://doi.org/10.2514/6.2017-4830.

[17] Y. Tang, S. Chen, W. Zhang, R. Shen, L. T. DeLuca, Y. Ye, Mechanical modifications of paraffin-based fuels and the effects on combustion performance, Propellants, Explos., Pyrotech. 42 (11) (2017) 1268–1277. doi:https://doi.org/10.1002/prep.201700136.

[18] M. Ashby, R. Medalist, The mechanical properties of cellular solids, Metall. Trans. A 14 (9) (1983) 1755–1769. doi:https://doi.org/10.1007/BF02645546.

[19] M. F. Ashby, The properties of foams and lattices, Philos. Trans. R. Soc., A 364 (1838) (2006) 15–30. doi:https://doi.org/10.1098/rsta.2005.1678.

[20] A. H. Schoen, Infinite periodic minimal surface without self-Intersections, Electron. Res. Cent. Camb., MA, NASA TN D-5541 (May, 1970).

[21] C. Z. Yan, L. Hao, A. Hussein, D. Raymont, Evaluations of cellular lattice structures manufactured using selective laser melting, Int. J. Mach. Tools Manuf. 62 (2012) 32–38. doi:https://doi.org/10.1016/j.ijmachtools.2012.06.002.

[22] Z. Qin, G. S. Jung, M. J. Kang, M. J. Buehler, The mechanics and design of a lightweight three-dimensional graphene assembly, Sci. Adv. 3 (1) (2017) 1–9. doi:https://doi.org/10.1126/sciadv.1601536.

[23] I. Maskery, L. Sturm, A. Aremu, A. Panesar, C. Williams, C. Tuck, R. Wildman, I. Ashcroft, R. Hague, Insights into the mechanical properties of several triply periodic minimal surface lattice structures made by polymer additive manufacturing, Polym. 152 (2018) 62 – 71. doi:https://doi.org/10.1016/j.polymer.2017.11.049.

[24] M. A. Hitt, Survey of applications of additively manufactured grains in hybrid rocket motors, in: 2018 Jt. Propuls. Conf., Cincinnati, OH, 2018, pp. 1–6. doi:https://doi.org/10.2514/6.2018-4712.

[25] S. A. Whitmore, Z. W. Peterson, S. D. Eilers, Comparing hydroxyl terminated polybutadiene and acrylonitrile butadiene styrene as hybrid rocket fuels, J. Propul. Power 29 (3) (2013) 582–592. doi:https://doi.org/10.2514/1.B34382.

[26] M. McFarland, E. Antunes, Small-scale static fire tests of 3D printing hybrid rocket fuel grains produced from different materials, Aerosp. 6 (7) (2019) 1–11. doi:https://doi.org/10.3390/aerospace6070081.

[27] J. McCulley, A. Bath, S. A. Whitmore, Design and testing of FDM manufactured paraffin-abs hybrid rocket motors, in: 48th AIAA/ASME/SAE/ASEE Jt. Propuls. Conf. Exhib., Atlanta, GA, 2012, pp. 1–24. doi:https://doi.org/10.2514/6.2012-3962.

[28] D. Armold, J. E. Boyer, K. Kuo, J. K. Fuller, J. Desain, T. J. Curtiss, Test of hybrid rocket fuel grains with swirl patterns fabricated using rapid prototyping technology, in: 49th AIAA/ASME/SAE/ASEE Jt. Propuls. Conf., San Jose, CA, 2013, pp. 1–14. doi:https://doi.org/10.2514/6.2013-4141.

[29] D. M. Armold, J. E. Boyer, B. McKnight, K. Kuo, J. Desain, B. B. Brady, J. Fuller, T. J. Curtiss, Testing of Hybrid Rocket Fuel Grains at Elevated Temperatures with Swirl Patterns Fabricated Using Rapid Prototyping Technology, in: 50th AIAA/ASME/SAE/ASEE Jt. Propuls. Conf., Cleveland, OH, 2014, pp. 1–13. doi:https://doi.org/10.2514/6.2014-3754.

[30] C. Paravan, R. Bisin, S. Carlotti, F. Maggi, L. Galfetti, Diagnostics for entrainment characterization in liquefying fuel formulations, in: 2018 Jt. Propuls. Conf., Cincinnati, OH, 2018, pp. 1–12. doi:https://doi.org/10.2514/6.2018-4663.

[31] C. Paravan, L. Galfetti, C. Paravan, R. Bisin, F. Piscaglia, Combustion processes in hybrid rockets, Int. J. Energ. Mater. Chem. Propul. 18 (3) (2019) 255–286. doi:https://doi.org/10.1615/intjenergeticmaterialschemprop.2019027834.

[32] K. M. Boronowsky, Non-homogenous hybrid rocket fuel for enhanced regression rates utilizing partial entrainement, Master's thesis, Dep. of Mech. Aerosp. Eng., San Jose State Univ., San Jose, CA (2011).

[33] B. J. Wang, S. J. Severtson, A. Stein, Significant and concurrent enhancement of stiffness, strength, and toughness for paraffin wax through organoclay addition, Adv. Mater. 18 (12) (2006) 1585–1588. doi:https://doi.org/10.1002/adma.200502615.

[34] M. Kobald, C. Schmierer, H. Ciezki, S. Schlechtriem, E. Toson, L. T. De Luca, Evaluation of paraffin-based fuels for hybrid rocket engines, in: 50th

AIAA/ASME/SAE/ASEE Jt. Propuls. Conf., Cleveland, OH, 2014, pp. 1–14. doi:https://doi.org/10.2514/6.2014-3646.

[35] S. Kim, H. Moon, J. Kim, J. Cho, Evaluation of paraffin polyethylene blends as novel solid fuel for hybrid rockets, J. Propul. Power 31 (6) (2015) 1750–1760. doi:https://doi.org/10.2514/1.B35565.

[36] R. Kumar, P. A. Ramakrishna, Studies on EVA-based wax fuel for launch vehicle applications, Propellants, Explos., Pyrotech. 41 (2) (2016) 295–303. doi:https://doi.org/10.1002/prep.201500172.

[37] M. Boiocchi, P. Milova, L. Galfetti, L. Di Landro, A. K. Golovko, A wide characterization of paraffin-based fuels mixed with styrene-based thermoplastic polymers for hybrid propulsion, in: Prog. Propuls. Phys., Vol. 8, 2016, pp. 241–262. doi:https://doi.org/10.1051/eucass/201608241.

[38] L. Galfetti, L. Merotto, M. Boiocchi, F. Maggi, L. T. DeLuca, Experimental investigation of paraffin-based fuels for hybrid rocket propulsion, in: Prog. Propuls. Phys., Vol. 4, 2013, pp. 59–74. doi:https://doi.org/10.1051/eucass/201304059.

[39] S. Ryu, S. Han, J. Kim, H. Moon, J. Kim, S. W. Ko, Tensile and compressive strength characteristics of aluminized paraffin wax fuel for various particle size and contents, J. Korean Nucl. Soc. Propuls. Eng. 20 (5) (2016) 70–76. doi:https://doi.org/10.6108/kspe.2016.20.5.070.

[40] K. Veale, M. J. Brooks, J. Pitot, Structural performance of large scale paraf-

974   fin wax based fuel grains, in: 51st AIAA/SAE/ASEE Jt. Propuls. Conf., Or-

975   lando, FL, 2015, pp. 1–8. doi:https://doi.org/10.2514/6.2015-3942.

976 [41] K. Veale, S. Adali, J. Pitot, C. Bemont, The structural properties

977   of paraffin wax based hybrid rocket fuels with aluminium particles,

978   Acta Astronaut. 151 (2018) 864–873. doi:https://doi.org/10.1016/

979   j.actaastro.2018.07.042.

980 [42] M. J. Kang, High performance curtain wall mullion section design with vari-

981   ous densities of gyroid, Master's thesis, Civ. Environ. Eng. Dept., Mass. Inst.

982   Technol., Camb., MA (2016).

983 [43] A. L. Olivares, È. Marsal, J. A. Planell, D. Lacroix, Finite element study

984   of scaffold architecture design and culture conditions for tissue engineer-

985   ing, Biomat. 30 (30) (2009) 6142–6149. doi:https://doi.org/10.1016/

986   j.biomaterials.2009.07.041.

987 [44] M. Wohlgemuth, N. Yufa, J. Hoffman, E. L. Thomas, Triply periodic bi-

988   continuous cubic microdomain morphologies by symmetries, Macromol.

989   34 (17) (2001) 6083–6089. doi:https://doi.org/10.1021/ma0019499.

990 [45] D. Li, W. Liao, N. Dai, G. Dong, Y. Tang, Y. M. Xie, Optimal design and

991   modeling of gyroid-based functionally graded cellular structures for additive

992   manufacturing, CAD Comput.-Aided Des. 104 (2018) 87–99. doi:https:

993   //doi.org/10.1016/j.cad.2018.06.003.

994 [46] Sasol website, products and applications, microcristallyne

995   waxes, https://www.sasolwax.com/fileadmin/sasolwax/

996 `Personal_Care_Waxes_and_Petroleum_jellies.pdf`, accessed: 997 2019-09.

[47] M. Kobald, E. Toson, H. Ciezki, S. Schlechtriem, S. Di Betta, M. Coppola, L. DeLuca, Rheological, optical, and ballistic investigations of paraffin-based fuels for hybrid rocket propulsion using a two-dimensional slab-burner, in: Prog. Propuls. Phys., Vol. 8, 2016, pp. 263–282. `doi:https://doi.org/10.1051/eucass/201608263`.

[48] M. Grosse, Effect of a diaphragm on performance and fuel regression of a laboratory scale hybrid rocket motor using nitrous oxide and paraffin, in: 45th AIAA/ASME/SAE/ASEE Jt. Propuls. Conf. Exhib., Denver, CO, 2009, pp. 1–25. `doi:https://doi.org/10.2514/6.2009-5113`.

[49] Merck website, products, `https://www.sigmaaldrich.com/catalog/product/aldrich/282863?lang=it&region=IT`, accessed: 2019-09.

[50] Merck website, products, `https://www.sigmaaldrich.com/catalog/product/aldrich/432431?lang=it&region=IT`, accessed: 2019-09.

[51] Prusa website, `https://www.prusa3d.it/`, accessed: 2019-05.

[52] Filoalfa website, `https://www.filoalfa3d.com/gb/content/15-nylon`, accessed: 2019-09.

[53] S. Farah, D. G. Anderson, R. Langer, Physical and mechanical properties of PLA, and their functions in widespread applications - A comprehensive review, Adv. Drug Delivery Rev. 107 (2016) 367–392. `doi:https://doi.org/10.1016/j.addr.2016.06.012`.

61

[54] S. A. Whitmore, S. D. Walker, D. P. Merkley, M. Sobbi, High regression rate hybrid rocket fuel grains with helical port structures, J. Propul. Power 31 (6) (2015) 1727–1738. doi:https://doi.org/10.2514/1.B35615.

[55] Y. Jia, H. He, X. Peng, S. Meng, J. Chen, Y. Geng, Preparation of a new filament based on polyamide-6 for three-dimensional printing, Polym. Eng. Sci. 57 (12) (2017) 1322–1328. doi:https://doi.org/10.1002/pen.24515.

[56] Int. Organ. Stand., ISO 604:2002 Plastics - Determination of compressive properties (2012), https://www.iso.org/standard/31261.html.

[57] F. Piscitelli, G. Saccone, A. Gianvito, G. Cosentino, L. Mazzola, Characterization and manufacturing of a paraffin wax as fuel for hybrid rockets, Propuls. Power Res. 7 (3) (2018) 218–230. doi:https://doi.org/10.1016/j.jppr.2018.07.007.

[58] Netzsch website, https://www.netzsch-thermal-analysis.com/en/products-solutions/simultaneous-thermogravimetry-differential-scanning-calorimetry/sta-449-f5-jupiter/, accessed: 2019-09.

[59] W. W. Wendlandt, Thermal methods of analysis, 2nd Edition, New York, Wiley-Interscience, 1974.

[60] S. Wu, Polymer Interface and Adhesion, 1st Edition, New York, CRC Press, 1982. doi:https://doi.org/10.1201/9780203742860.

[61] S. W. Ip, J. M. Toguri, The equivalency of surface tension, surface energy and surface free energy, J. Mater. Sci. 29 (3) (1994) 688–692. doi:https://doi.org/10.1007/BF00445980.

[62] H. W. Fox, W. A. Zisman, The spreading of liquids on low energy surfaces. 1. polytetrafluoroethylene, J. Colloid Sci. 5 (6) (1950) 514–531. `doi:https://doi.org/10.1016/0095-8522(50)90044-4`.

[63] D. K. Owens, R. C. Wendt, Estimation of the surface free energy of polymers, J. Appl. Polym. Sci. 13 (8) (1969) 1741–1747. `doi:https://doi.org/10.1002/app.1969.070130815`.

[64] Femap website, `https://www.plm.automation.siemens.com/global/it/products/simcenter/femap.html`, accessed: 2019-07.

[65] Siemens documentation, Basic Nonlinear Analysis User's Guide, `https://docs.plm.automation.siemens.com/data_services/resources/nxnastran/11/help/tdoc/en_US/pdf/bas_nonlinear.pdf`, accessed: 2019-09.

[66] Siemens documentation, Element Library Reference, `https://docs.plm.automation.siemens.com/data_services/resources/nxnastran/10/help/en_US/tdocExt/pdf/element.pdf`, accessed: 2019-09.

[67] S. Jose, P. S. Thomas, S. Thomas, J. Karger-Kocsis, Thermal and crystallisation behaviours of blends of polyamide 12 with styrene-ethylene/butylene-styrene rubbers, Polymer 47 (18) (2006) 6328–6336. `doi:https://doi.org/10.1016/j.polymer.2006.07.002`.

[68] N. V. Muravyev, K. A. Monogarov, D. Prokopyev, A. A. Bragin, L. Galfetti, L. T. Deluca, A. N. Pivkina, Macro- vs Microcrystalline Wax: Interplay of Evaporation and Decomposition under Pressure Variation, Energy

and Fuels 31 (8) (2017) 8534–8539. doi:https://doi.org/10.1021/acs.energyfuels.7b00895.

[69] J. D. Menczel, L. Judovits, R. B. Prime, H. E. Bair, M. Reading, S. Swier, Differential scanning calorimetry (dsc), in: J. D. Menczel, R. B. Prime (Eds.), Thermal Analysis of Polymers, John Wiley and Sons, Ltd, 2008, Ch. 2, pp. 7–239. doi:https://doi.org/10.1002/9780470423837.

[70] R. Bisin, C. Paravan, A. Verga, L. Galfetti, An Innovative Strategy for Paraffin-based Fuels Reinforcement: Part II, Ballistic Characterization, in: 8th Eur. Conf. for Aeronaut. and Space Sci. (EUCASS), Madrid, ES, 2019, pp. 1–9. doi:https://doi.org/10.13009/EUCASS2019-728.

[71] Prusa website, filament PLA, https://shop.prusa3d.com/fotky/PLA_TechSheet_ENG.pdf, accessed: 2020-06.

[72] Prusa website, filament ASA/ABS, https://shop.prusa3d.com/en/filament/134-orange-easyabs-filament-1kg.html, accessed: 2020-06.

[73] Stratasys website, materials, nylon 6, https://www.stratasys.com/materials/search/fdm-nylon-6, accessed: 2020-06.

[74] Int. Organ. Stand., ISO 13314:2011 Mechanical testing of metals - Ductility testing - Compression test for porous and cellular metals (2011), https://www.iso.org/standard/53669.html.